Tandem Nanostructures: A Prospective Platform for Photoelectrochemical Water Splitting

Jun Liu, Huaping Zhao, Zhijie Wang,* Thomas Hannappel, Ulrike I. Kramm, Bastian J. M. Etzold, and Yong Lei*

A platform for efficient photoelectrochemical (PEC) water splitting must fulfil different requirements: the absorption of the solar spectrum should be maximized in use for charge carrier generation. To avoid recombination, fast separation of charge carriers is required and the energetic positions of the band structure(s) must be optimized with respect to the water splitting reactions. In these respects, constructing tandem nanostructures with rationally designed nanostructured units offers a potential opportunity to break the performance bottleneck imposed by the unitary nanostructure. So far, quite a few tandem nanostructures have been designed, fabricated, and employed to improve the efficiency of PEC water splitting, and significant achievements have been realized. This review focuses on the current advances in tandem nanostructures for PEC water splitting. Firstly, the state of the art for tandem nanostructures applied in PEC water splitting is summarized. Secondly, the advances in this field and advantages arising of employing tandem nanostructures for PEC water splitting are outlined. Subsequently, different types of tandem nanostructures are reviewed, including core-shell tandem nanostructured photoelectrode, the two-photoelectrode tandem cell, and the tandem nanostructures of plasmon related devices for PEC water splitting. Based on this, the future perspective of this field is proposed.

1. Introduction

With the rapid development of world economy and the increase of global population, the energy crisis and environmental pollution have gradually become the key challenges for the sustainable development of mankind. An artificial photosynthesis for converting solar energy into chemical energy can offer an effective method to solve the worldwide energy crisis.[1] Since Fujishima and Honda reported the utilization of TiO_2 to generate H_2 photoelectrochemically in 1972,[2] photoelectrochemical (PEC) water splitting has attracted considerable concerns for its environmental friendliness.[3] On account of the less dependence on the electric energy, the utilization of the maximum energy of solar energy, and the reusability of photoelectrode, PEC water splitting has the integrated advantages of electrochemical water splitting and photocatalytic water splitting.[4]

During the past decades, plenty of researchers contribute to the development of PEC water splitting. Fabricating heterojunctions has been revealed as an effective

J. Liu
Guangdong-Hong Kong Joint Laboratory for Water Security
Engineering Research Center of Ministry of Education on Groundwater
Pollution Control and Remediation
Center for Water Research
Advanced Institute of Natural Sciences
Beijing Normal University at Zhuhai
Zhuhai 519087, P. R. China

H. Zhao, Y. Lei
Fachgebiet Angewandte Nanophysik
Institut für Physik & IMN MacroNano
Technische Universität Ilmenau
98693 Ilmenau, Germany
E-mail: yong.lei@tu-ilmenau.de

The ORCID identification number(s) for the author(s) of this article can be found under https://doi.org/10.1002/solr.202200181.

Z. Wang
Key Laboratory of Semiconductor Materials Science
Beijing Key Laboratory of Low Dimensional Semiconductor Materials and Devices
Institute of Semiconductors
Chinese Academy of Sciences
Beijing 100083, P. R. China
E-mail: wangzj@semi.ac.cn

T. Hannappel
Fundamentals of Energy Materials
Institute of Physics
Technische Universität Ilmenau
98693 Ilmenau, Germany

U. I. Kramm
Department of Chemistry, Catalysts and Electrocatalysts group
Technical University of Darmstadt
64287 Darmstadt, Germany

B. J. M. Etzold
Department of Chemistry
Ernst-Berl-Institut für Technische und Makromolekulare Chemie
Technical University of Darmstadt
64287 Darmstadt, Germany

strategy to promote the separation of charge carriers in the solar-driven water splitting process.[5] The development of sensitized materials responded to the near-infrared (NIR) region has widened the light absorption range in solar spectrum.[6] And PEC water splitting powered only by solar energy, namely, self-biased PEC water splitting, is of significant interest for efficiently utilizing solar energy without the dependence on electricity.[7] The decoration of cocatalysts has improved the efficiency by boosting the reaction kinetics.[8] The surface passivation layer of metal oxides could reduce charge recombination at surface states, increase the reaction kinetics, and protect the semiconductor from chemical corrosion, which is beneficial for achieving highly-efficient water splitting.[9] The doping of extrinsic elements into the crystal lattice can remodel the energy band structure, thus influence the efficiency.[10] The nanostructured photoelectrodes could improve the light absorption, and by an improved specific surface area shorten the distance that charge carriers need to migrate to the surface reaction sites, etc., which could be the universal strategy to improve the performance of PEC water splitting.[11] Due to the antenna effect when absorbing solar radiation through a nanowire array, there is also an implied light concentration leading to an improved Fermi-level splitting and, thus, a higher voltage.[11c]

Though the mentioned above strategies have promoted the development of PEC water splitting to a great extent, the industrialized application of it still faces the challenge on account of the cost, efficiency and availability. Tandem nanostructures consisting of rationally designed nanostructured units represent an effective photoelectrode configuration to break the performance bottleneck imposed by the unitary nanostructure, which include the following types: 1) core-shell nanostructures for single photoelectrode, which combines the highly-absorbent material (such as Si,[12] III-V compound semiconductors,[11c,13] etc.) as the core, while the metal oxides shell as buffer and protective layer,[12a,13a,14] and the cocatalyst anchored on the metal oxides shell[15]; 2) two-photoelectrode tandem cell assembled in parallel or in monolithic to realize the highly-efficient or unassisted water

splitting, where the photocathode produces hydrogen with the photoanode generating oxygen simultaneously, and the self-driven bias depends on the difference of aligned Fermi levels in photocathode and photoanode, respectively[16]; 3) tandem nanostructures of plasmon related devices for the improvement of PEC water splitting, where nanostructures of noble metals like Au or Ag are surrounded by semiconductors in a layered tandem structure[17] or in a Janus heteronanostructure,[3b,18] and the specific mechanisms of plasmons such as hot electron injections, local electric field enhancement, and resonance energy transfer could be clarified more clearly in the regular structure. The overview of the tandem nanostructures schematics and tandem devices for PEC water splitting is shown in **Figure 1**.

Though nanostructures for PEC water splitting have been reviewed by a few groups, there is still lack of a specific review focusing on tandem nanostructures for PEC water splitting. In this review, we provide a comprehensive overview of recent advances in developing tandem nanostructures for PEC water splitting. We first summarize the advances and advantages of tandem nanostructures for PEC water splitting. Then we highlight three main types of tandem nanostructures that are developed for PEC water splitting and analyze their synergic effects on optimizing PEC performance. Finally, we provide an outlook on challenges and perspectives associated with tandem nanostructures for PEC water splitting.

2. The Advances and Advantages of Tandem Nanostructures for PEC Water Splitting

The tandem nanostructures possess integrated advantages of every components, which could optimize the light absorption, accelerate the generation and separation of charge carriers, and realize a highly-efficient and possibly even unassisted water splitting. On the contrary, the unitary nanostructure scarcely satisfies all these above-mentioned high-performance requirements at the same time. Thus, tandem nanostructures have been widely
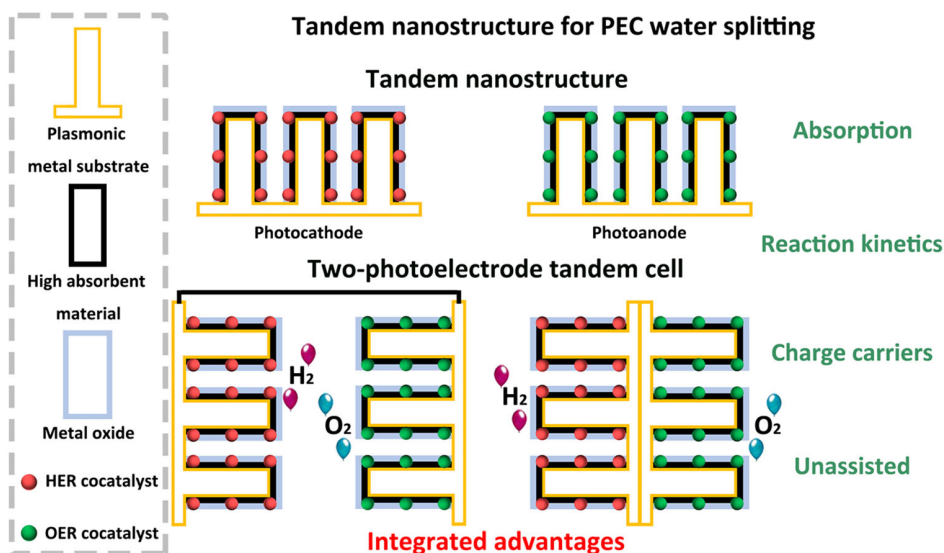

Figure 1. The overview of tandem nanostructures schematics and tandem devices for PEC water splitting.

employed in PEC water splitting, and significant achievements have been realized in the past years.

2.1. Optimizing the Light Absorption

A first step in this direction was made by Dotan et al. who used a V-shape design of hematite photoanodes that were enhanced in absorption by using a reflective substrate, and the water photo-oxidation current density reached up to $4\,mA\,cm^{-2}$ at 1.63 V (vs RHE).[19] Ansari et al. fabricated a tandem photoanode consisting of a layer of Cu_2ZnSnS_4 (CZTS) nanoparticles deposited on a CdS/TiO_2 heterostructure thin film grown on FTO substrate for PEC hydrogen generation at the counter electrode. This $CZTS/CdS/TiO_2/FTO$ tandem structure resulted in different band level positions, which enhanced the optical absorption in the visible region and also led to highly-efficient separation of photo-generated charge carriers. A substantial enhancement (39 times) in the PEC activity has been demonstrated for the $CZTS/CdS/TiO_2/FTO$ photoanode as compared to TiO_2/FTO photoanode, which is attributed to the cascade band gap from 3.2 to 1.7 eV and the formation of heterojunction at interfaces.[20] Bai et al. constructed self-driven tandem PEC cells based on Cu_2O/Cu_2S photocathodes and ZnO/CdS photoanodes, and the tandem cell had a photoconversion efficiency of 0.38% at a zero bias. The Cu_2S layer caused an increase in cathodic photocurrent and reduce hydrogen evolution overpotential because of the enhancement in light absorption and charge transfer properties.[21] Narkeviciute et al. prepared core-shell $Si–Ta_3N_5$ tandem photoanodes for PEC water oxidation, where nanostructured $Si–Ta_3N_5$ increased the electrochemical surface area and the incident light absorption due to light trapping effect.[22] Besides, this core-shell dual-absorber design strategy can boost the efficiency by improving the light absorption. As a result, higher photocurrents were realized compared to planar devices.

2.2. Accelerating the Generation and Separation of Charge Carriers

Cao et al. fabricated multiple $CaFe_2O_4/ZnFe_2O_4$ p–n junction nanostructure by a pulsed laser deposition method.[23] It was demonstrated that the multiple p–n junction structures could enhance the photocurrent density and favorably shift the onset potential. The PEC cell based on 20-junction photoelectrodes showed an open circuit photovoltage up to 0.97 V, which is only 0.13 V for PEC cell with a single p–n junction photoelectrode (**Figure 2**a,b). A multiple-junction band structure model is proposed to describe the behavior of $CaFe_2O_4/ZnFe_2O_4$ multiple-junction photoelectrodes. The photocurrent density of multiple-junction photoelectrodes is determined by the
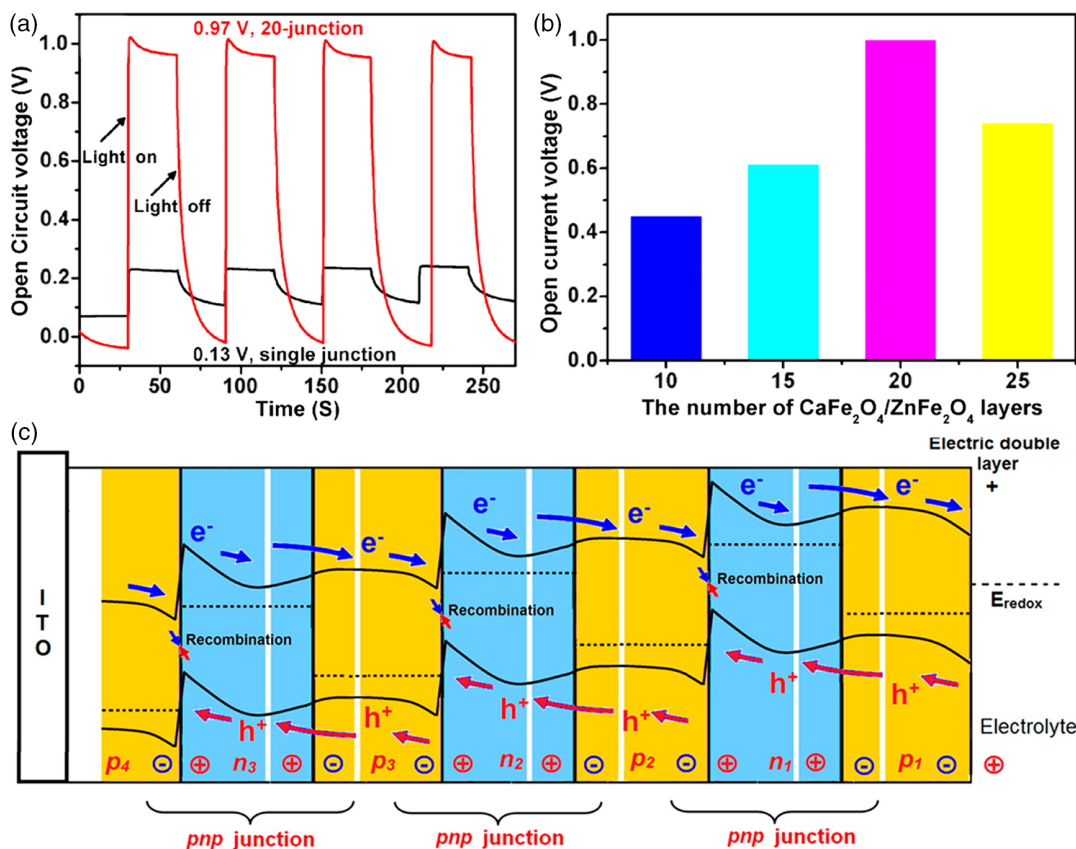
Figure 2. a) V–t curve of p–$CaFe_2O_4$/n–$ZnFe_2O_4$ junction electrode (black line) and multilayer p–$CaFe_2O_4$/n–$ZnFe_2O_4$ junction electrode (red line), b) Open circuit photovoltage of different multilayer p–$CaFe_2O_4$/n–$ZnFe_2O_4$ junction electrodes and c) Schematic of a multilayer p–n–p junction electrode in the electrolyte under light irradiation. Reproduced with permission.[23] Copyright 2013, American Chemical Society.

photocurrent density generated by the single p–n–p junction because the carrier of a single p–n–p junction can recombine only with the carrier from the neighboring p–n–p junction (Figure 2c). Wang et al. constructed a tandem PEC cell with two photoactive electrodes, where the photoanode is composed of a pseudocapacitive WO_3 nanoflake film sensitized with visible-light responsive zeolitic-imidazolate-framework-67 (ZIF-67), and the photocathode is constituted with a Z-scheme $BiVO_4$-black phosphorus (BP) heterojunction that can broaden the light absorption to NIR region as well as maintain the strong redox ability to fasten hydrogen evolution reaction after effective charge separation.[24] Deliberately, the alignment of Fermi level between the as-prepared WO_3-ZIF-67 photoanode and $BiVO_4$-BP photocathode provided a reversible electron storage property to enable light-induced charge storing and on-demand release in the dark for the application of unassisted overall water splitting.

2.3. Realizing Highly Efficient and Unassisted Water Splitting

Shao et al. constructed a spatially separated organic-inorganic hybrid Z-schematic PEC cell for unassisted overall water splitting by wiring inorganic ZnO nanorod arrays as photoanode and organic poly(3-hexylthiophene):[6,6]-phenyl-C_{61}-butyric acid (P_3HT: PCBM) as photocathode in a tandem manner.[25] In this system (Figure 3), the catalytic centers for reduction and oxidation were spatially separated, which not only minimized the undesirable back-reaction but also separated the photocatalytic products. Such a system could achieve unassisted solar-driven overall water splitting without using any sacrificial agents in the solution. Ghorpade et al. chose Cu_3SbS_4 carbon quantum dots (CQD) modified NiO nanosheet photocathode and $CuSbS_2$ CQD-modified TiO_2 nanorod photoanode for water reduction and oxidation reactions, respectively, that allowed maximum solar energy harvesting under visible light illumination.[26] Additionally, surface passivation with a thin layer of ZnS was used to improve the stability of photoelectrodes. Thus, the above system realized efficient and unassisted solar water splitting, and

the overall solar-to-hydrogen (STH) efficiency was ≈0.28%. Pan et al. introduced Cu dopants into CdS shell, and as a demonstration, the conductive nature of Au@CdS core-shell hybrid nanocrystals was changed from n– to p–type.[27] Finally, a tandem PEC cell was fabricated with undoped Au@CdS photoanode and Cu-doped Au@CdS photocathode, and displayed stable O_2 and H_2 evolution, respectively, giving a high O_2 evolution rate of 203 μmol h^{-1} cm^{-2} in unassisted PEC overall water splitting.

3. Core-Shell Tandem Nanostructured Photoelectrode for PEC Water Splitting

To construct a PEC water splitting system with high efficiency and stability, a photoelectrode material of abundance, low cost, and high efficiency is important. However, all discovered photoelectrode materials have more or less shortcomings, such as poor light absorption, high carrier recombination rate, sluggish surface redox reaction, or poor stability. Construction of core-shell configuration to form the heterojunction and favorable band bending for charge carriers generation and transportation has been demonstrated as an effective strategy to overcome these shortcomings, where a shell coating can endow a photoelectrode with improved activity and stability.[28] At present, many kinds of core-shell photoelectrodes with various composition and properties have been developed for PEC water splitting. In this section, we highlight the compositions of core-shell photoelectrode.

3.1. The Core of High Absorbent Material

Generally, an ideal core material in photoelectrodes should possess the following characteristics: 1) Suitable band structure and bandgap, which dictate the driving force and energy conversion efficiency of PEC reactions. According to the redox potential of H_2O, the theoretical minimum bandgap for a semiconductor to drive water splitting is 1.23 eV. However, due to the thermodynamic energy, losses (0.3–0.4 eV) and the overpotential
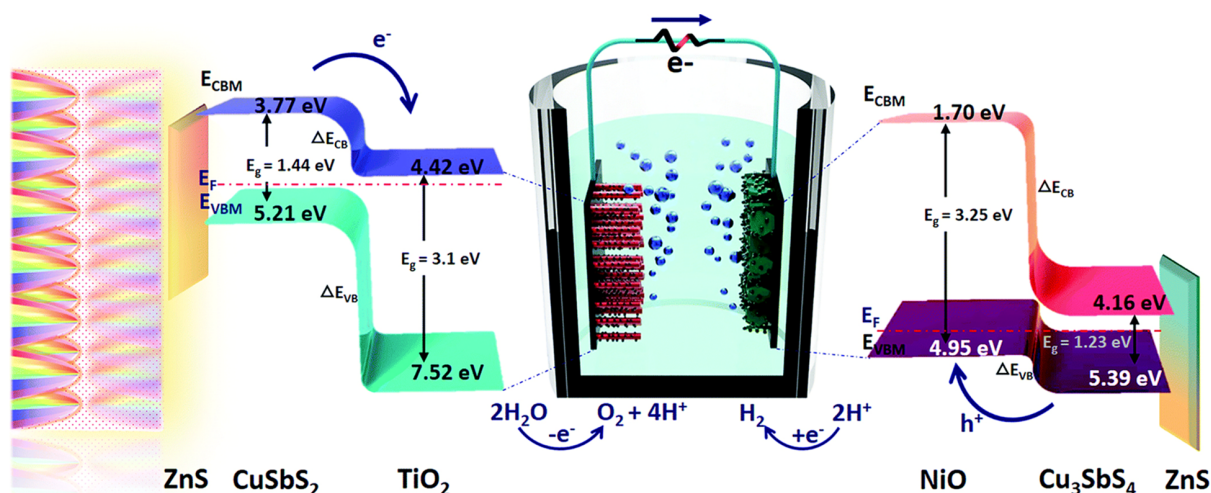

Figure 3. Overall unassisted water-splitting mechanism of PEC H_2 and O_2 generation using the NiO/Cu_3SbS_4/ZnS photocathode and TiO_2/$CuSbS_2$/ZnS photoanode along with their respective energy levels and electron-hole-transfer processes occurring in a tandem configuration. Reproduced with permission.[26] Copyright 2018, The Royal Society of Chemistry.

requirements for surface reaction kinetics (0.4–0.6 eV), a minimum bandgap should be about 1.8 eV. Furthermore, ultraviolet light makes up only 5% while visible and infrared light account for nearly 95% of sunlight. Therefore, to improve the STH conversion efficiency, a semiconductor with suitable bandgap and appreciable light response beyond the violet region is required. **Figure 4** shows the bandgaps and band structures of typical semiconductors used as core materials in photoelectrode for water splitting[29]; 2) High charge carrier separation and migration efficiency. This is closely related to the intrinsic properties of the material and determines the number of charge carriers involved in the catalytic reaction; 3) Excellent catalytic activity and good stability against corrosion, which can avoid the recombination of carriers and increase the lifetime and efficiency of photoelectrode; and 4) Additionally, the price of the core materials also needs to be considered, which directly affects the industrial and large-scale applications of PEC water splitting.

With the progress of semiconductor technology and material science, numerous visible-light-responsive semiconductors as core material of photoelectrode have been developed. The representative materials include Si and III-V compound semiconductors, which possess tunable bandgaps for light absorption in the spirit of the well-known band gap engineering including relatively narrow band gaps, e.g., 1.1 eV for Si, 1.05 eV for GaInAsP lattice-matched to InP, 1.35 eV for InP, 1.42 eV for GaAs, or 1.90 to 2.23 eV for AlGaInP lattice-matched to GaAs.[28b,29] For example, the GaAs- and Si-based core-shell PEC photoelectrodes had been reported by Cui's and Jaramillo's groups, respectively (**Figure 5**).[13a,22] However, these materials usually suffer from corrosion during the PEC reactions. Therefore, surface treatments and/or protective layer coatings are necessary to improve their stability. Moreover, many ceramic oxides (such as TiO_2, Cu_2O, CuO, $BiVO_4$, WO_3, and Fe_2O_3) also have been employed as photoelectrode materials during the past decade, due to the low costs and narrow bandgaps.[29,30] However, the conduction band (CB) and valence band (VB) edges of these materials have unfavored positions compared to the water redox potentials. To drive water splitting by utilizing solar energy, bandgap engineering and surface engineering have been conducted to optimize the electronic and optical properties of these materials.[31]

Some II–VI semiconductors, such as CdS, CdTe, CdSe, and ZnTe, also have narrow bandgaps, and are investigated as photoelectrode materials.[32] However, these II–VI semiconductors usually have poor water redox reaction kinetics, which can cause charge carrier accumulation at the surface and lead to serious electrode corrosion. Therefore, constructing heterojunctions or coating surface passivation layers are commonly employed to reduce surface recombination, increase reaction kinetics, and protect photoelectrodes. For instance, to restrain photocorrosion and improve charge separation/transportation efficiency of a CdS core, Zhang and coworkers fabricated CdS–ZnS core-shell photoelectrodes, and obtained a high photocurrent density of 7.8 mA cm^{-2} with incident photon to electron conversion efficiency (IPCE) values above 35% at a potential of 0 V vs SCE under 300 nm. (**Figure 6**a).[33] Compared to the rapid photocurrent decay of CdS, the CdS–ZnS core-shell photoelectrode maintained high photostability. Additionally, Ta_3N_5 with a bandgap of 2.1 eV is visible-light-responsive, and thus is a potential candidate of core material for high efficient photoelectrodes.[34] As shown in Figure 6b,c, Domen's group reported a highly conductive photoanode based on polycrystalline Ta_3N_5 nanorods (Ta_3N_5–NRs).[35] However, due to the low onset potential and poor stability, the best solar to hydrogen (STH) efficiency yet reported for Ta_3N_5-based photoanodes was only up to 2.7%. In view of this, a detailed numerical model based Ba-doped or undoped Ta_3N_5–NRs was devised, which can effectively predict various factors contributing to performance losses, such as optical effects, charge carrier recombination, and resistivity.[36]

Recently, a family of spinel ferrites with a general formula of MFe_2O_4 (M: Cu, Mg, Zn, etc.) had been explored as light absorber for PEC water splitting, owing to its narrow bandgap,
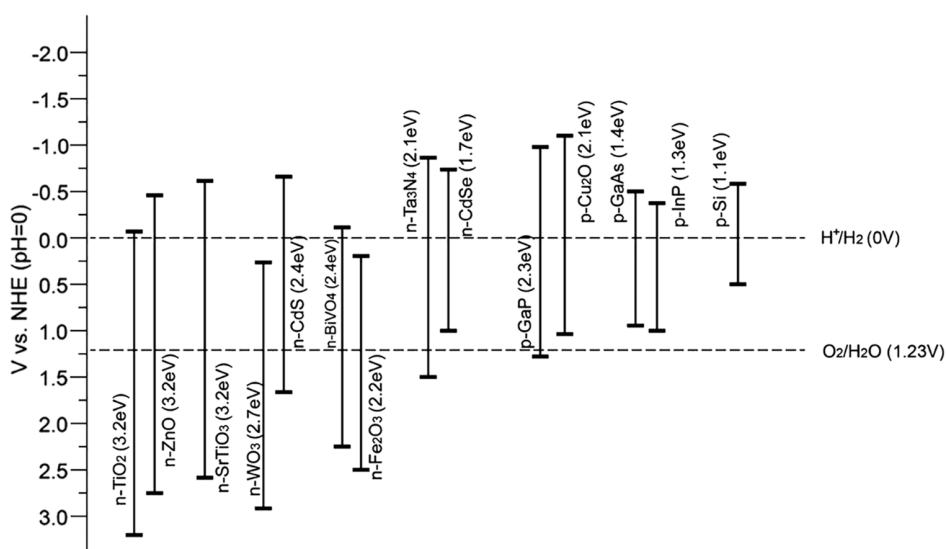

Figure 4. Schematic illustration of the energy bandgaps and band edges of commonly reported photoelectrode materials at pH = 0. Reproduced with permission.[29] Copyright 2017, The Royal Society of Chemistry.
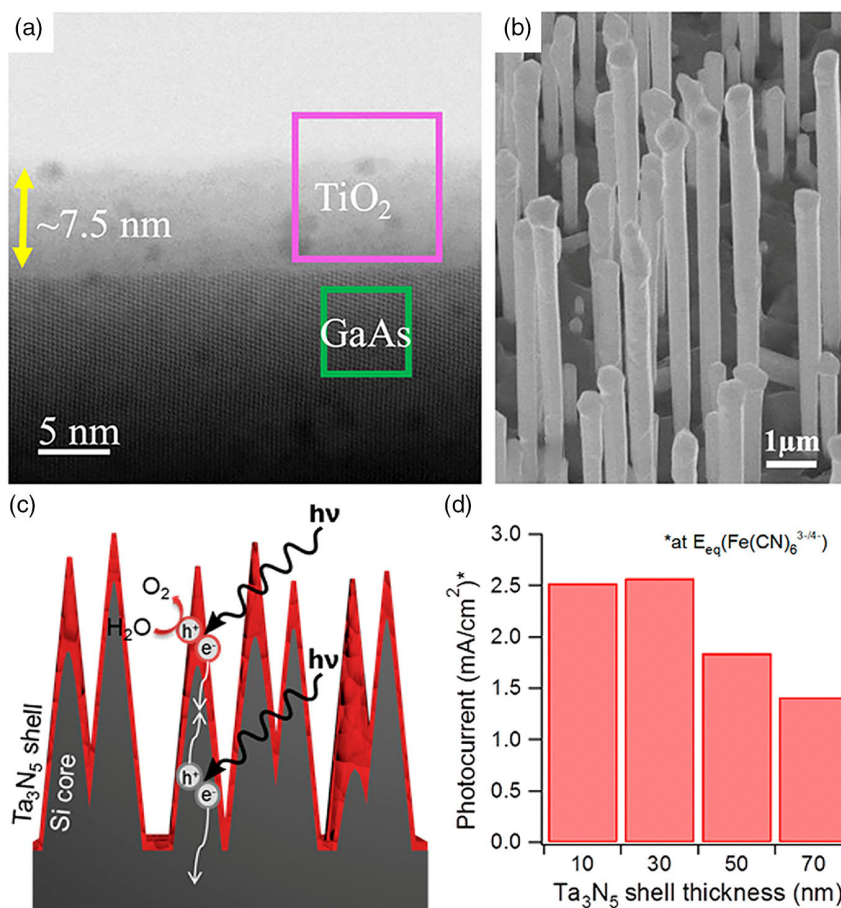
Figure 5. SEM a) and higher-magnification TEM b) images of the GaAs NW/TiO₂ photoelectrode. Reproduced with permission.[13a] Copyright 2021, American Chemical Society. c) Schematic illustration of charge transfer in Si/Ta₃N₅ core-shell photoanode. d) The photocurrent change of Si/Ta₃N₅ photoanode accompanied with different Ta₃N₅ shell thickness. Reproduced with permission.[22] Copyright 2016, American Chemical Society.

earth abundant elemental composition, and tunable optoelectronic properties (by changing the cation M).[39] However, the experimental photocurrents of these materials laid far below the theoretical values. Liu et al. fabricated a series of $CuFe_2O_4$ thin-film photoanodes, and revealed that the low photocurrents might be arisen from the strong Fermi level pinning, short hole diffusion length ($\approx$4 nm), and low charge collection efficiency (below 10%) during the catalytic reaction.[39d] In the past few years, Sb_2Se_3 and GeSe are also considered as new promising semiconductors for PEC water splitting, owing to their high optical absorption and theoretical maximum efficiency of $\approx$30%. Park et al. constructed an efficient and stable PEC system based on a bilayer nanostructured Sb_2Se_3 photocathode (Figure 6d), where the photocurrent density reached nearly 30 mA cm^{-2} at 0 V vs reversible hydrogen electrode (RHE), the IPCE was as high as 85.7% under 750 nm-light illumination, the Faradaic efficiency of the H_2 evolution reaction was over 90%, and it maintained nearly 100% of the initial photocurrent after 5 h in a pH 1 solution and 85% after 10 h when being operated in a pH 6.5 solution, attributing to the synergetic effects of the special construction and the favorable crystallographic orientation.[37] Similar to Sb_2Se_3, GeSe is a binary semiconductor with a narrow bandgap of 1.2 eV. To improve the stability and carrier separation

efficiency, Wang et al. designed GeSe-based photoelectrodes by coating GeSe with Cd-free Pt/C₆₀ pat.–TiO₂ fullerene composite materials (Figure 6e). The as-prepared photoelectrode showed a significantly enhanced long-term stability of 60 h, and finally a GeSe–BiVO₄ tandem cell for unbiased overall solar water splitting presented a STH efficiency of 1.37% and a long-term stability over 12 h.[38] The C₆₀ particle intermediate helped to build a bridge between the Pt catalysts and TiO₂ balls, contributing to accelerate electron transfer, avoid the self-reduction of TiO₂ balls, and decrease the accumulation of photoexcited carriers at interfaces. Additionally, metal sulfides with narrow bandgaps are another type of emerging core materials for photoelectrodes, such as Cu_2S and Cu_2BaSnS_4.[34,40] However, the STH efficiencies of sulfide-based photoelectrodes are still much lower than the theoretical values, indicating that there is still a lot of work to be done.

3.2. The Shell of Photoelectrodes with Different Functions

To construct a photoelectrode with high efficiency and stability, it has been recognized that a single type of core material is not enough to meet all requirements, i.e., light absorption, charge carrier separation, catalysis, and passivation. One of the best
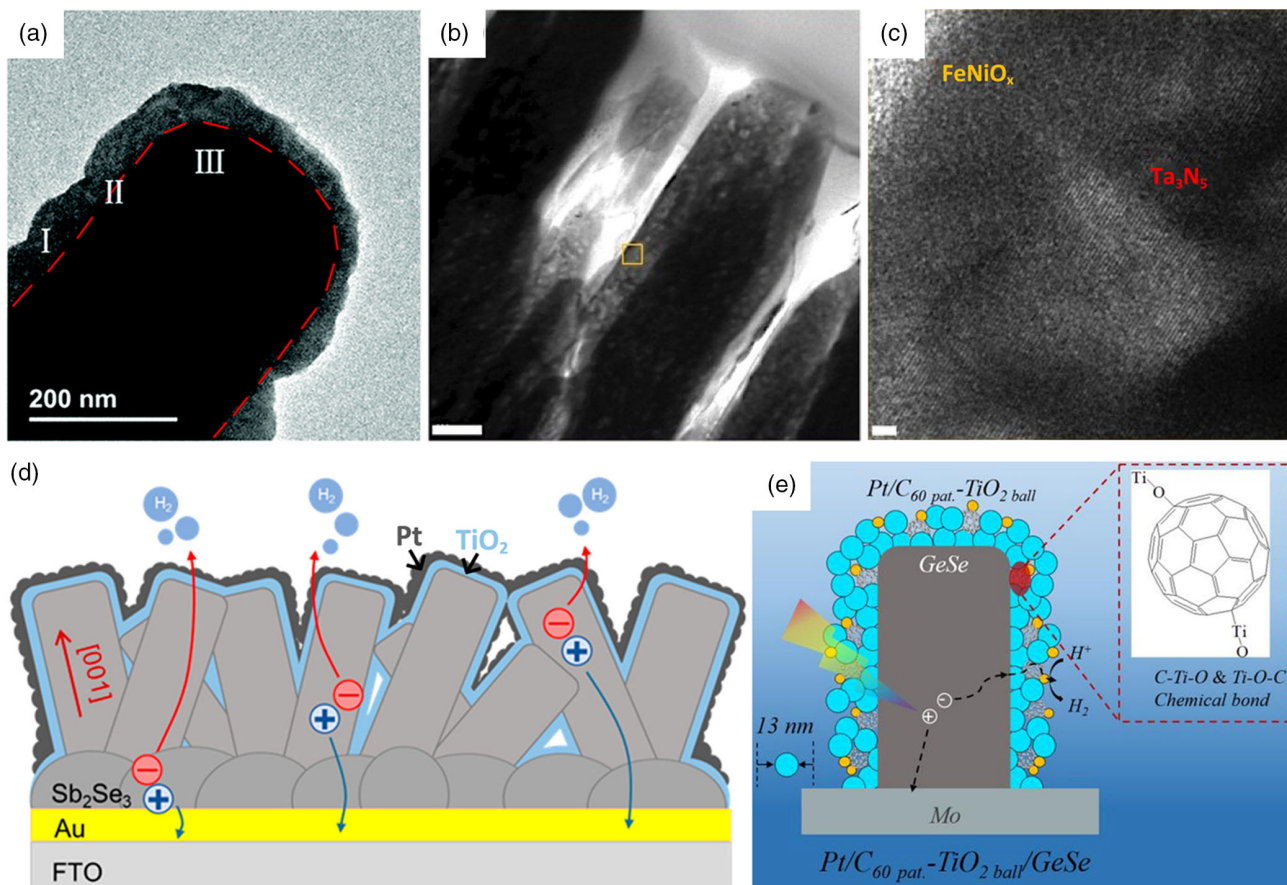
Figure 6. TEM images of a) CdS/ZnS,[33] and b,c) Ta$_3$N$_5$/FeNiO$_x$ core–shell nanorods.[35] Reproduced with permission.[33] Copyright 2015, The Royal Society of Chemistry. Reproduced with permission.[35] Copyright 2020, The Royal Society of Chemistry. Schematic diagrams of the carrier transfer pathways and PEC hydrogen generation process of d) Sb$_2$Se$_3$/TiO$_2$,[37] and e) GeSe/C$_{60\ pat.}$–TiO$_2$ ball/Pt photoelectrodes.[38] Reproduced with permission.[37] Copyright 2020, American Chemical Society. Reproduced with permission.[38] Copyright 2021, Elsevier.

strategies to realize these functionalities is to construct a core-shell photoelectrode that is to integrate the core materials with multifunctional shells.[11] The shell can be fabricated and optimized according to the characteristics of core materials so as to achieve complementary advantages and improve the overall STH efficiency.[28b] In this perspective, materials with suitable bandgaps and electronic properties can be coated on a photoelectrode for maximizing light absorption and charge separation, facilitating for fast and highly specific charge transfer, acting as passivation or protection layer for inhibiting corrosion. In this section, we highlight the representative functions of shell structure.

3.2.1. Passivation Layers or Protection Layers for Photoelectrode

During PEC water splitting reactions, the activity and stability of photoelectrode may decrease gradually due to corrosion. Generally, there are two types of corrosion of the photoelectrode. The first one arises from the reaction of the photoelectrode with the electrolyte. The second one is photocorrosion caused by the sluggish water splitting reactions. The photocorrosion can result in a severe accumulation of charge carriers on the surface of the

photoelectrodes, and thereafter the excess charge carriers may react with the base material of these photoelectrodes. Generally, Si, III–V semiconductors, metal oxides (like Cu$_2$O, BiVO$_4$), and metal chalcogenides (such as CdS) need to be protected when being used as photoelectrodes.[32a,41] To this end, constructing passivation layer outside the core materials has been widely applied. The main role of a passivation layer is to reduce the recombination of charge carriers at the interface of photoelectrodes and electrolytes, thereby improving the kinetics of desired reactions and preventing the core of the photoelectrode from corrosion.[28a]

Many materials have been used to fabricate the passivation layer, such as metal silicides, oxides, nitrides, and phosphides.[12a,42] Particularly, TiO$_2$ is the most widely used one, owing to its suitable band structure and intrinsic chemical stability. Kunturu et al. recently fabricated a photocathode based on Si/Cu$_2$O core-shell micropillar arrays (**Figure 7**a), in which the multifunctional overlayers of ZnO (25 nm) and TiO$_2$ (100 nm) were coated by a pulsed laser deposition method. The ZnO/TiO$_2$ overlayers act as a hole-selective passivation layer to resist the photocorrosion during the PEC water splitting reaction. As a result, the Si/Cu$_2$O photocathode exhibited an excellent PEC
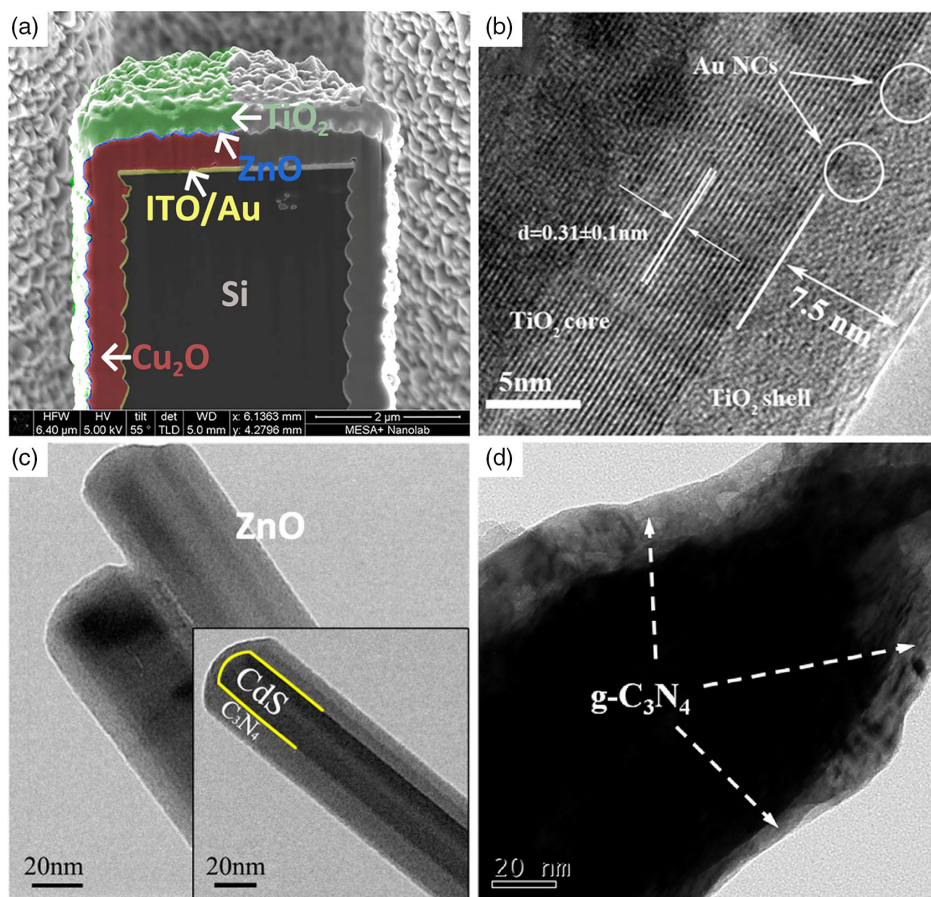
Figure 7. a) HR-SEM cross-sectional image of Si/ITO–Au/Cu₂O/ZnO/TiO₂ photocathode. Reproduced with permission.[14] Copyright 2019, American Chemical Society. TEM images of core-shell photoelectrodes: b) TiO₂@Au₂₅/TiO₂, Reproduced with permission.[43] Copyright 2020, American Chemical Society. c) CdS/g–C₃N₄, Reproduced with permission.[44c] Copyright 2013, American Chemical Society. and d) ZnO/g–C₃N₄. Reproduced with permission.[45] Copyright 2019, Elsevier.

performance with an optimal photocurrent of $7.5\,\mathrm{mA\,cm^{-2}}$ at 0 V vs RHE, a photovoltage of 0.85 V, and a stable operation for 75 h.[14] Moreover, to improve the stability of gold-based photoelectrodes, $TiO_2@Au25/TiO_2$ core-shell nanowire arrays had been fabricated by Yu and coworkers, where an ultrathin TiO_2 shell layer was coated on gold nanoclusters via atomic layer deposition (ALD), as shown in Figure 7b.[43] The TiO_2 shell could effectively restrict the growth and loss of gold nanoclusters on the surface of the nanowires during the PEC process. Finally, the $TiO_2@Au_{25}/TiO_2$ photoanode showed an excellent stability and the gaseous evolution remained unaltered after several hours runs.

Owing to its wide light response range and excellent physicochemical stability, $g–C_3N_4$ is another emerging material that can be used as a passivation layer to construct core-shell photoelectrode. So far, $g–C_3N_4$-based core-shell photoelectrodes have been fabricated for PEC water splitting, such as $Pt/g–C_3N_4/ZnO$, $CdS/g–C_3N_4$ (Figure 7c), and $TiO_2/g–C_3N_4$.[44] As shown in Figure 7d, Sun and coworkers synthesized a Co–Pi decorated $ZnO/g–C_3N_4$ core-shell nanorod arrays as the photoelectrode for PEC water splitting. The Co–Pi cocatalysts could assist the consumption of the photoinduced holes, pull the Fermi level potential of $g–C_3N_4@ZnO$ NRAs to the positive direction to induce the upward band bending at the band-edge position, and thus improve the stability of the PEC performance, and thus the stability and PEC activity were remarkably improved.[45]

Lead-halide perovskites have triggered the latest breakthrough in photovoltaic technology. Despite their great promise, their instability towards water even in the presence of low amounts of moisture makes them a priori and unsuitable for their direct use as light harvesters in aqueous solution for the hydrogen production through water splitting. As shown in **Figure 8**, Crespo-Quesada et al. used field's metal of a fusible InBiSn alloy to efficiently protect the perovskite from water while simultaneously allowing the photogenerated electrons to reach a Pt hydrogen evolution catalyst. As a result, a record photocurrent density of $-9.8\,\mathrm{mA\,cm^{-2}}$ at 0 V versus RHE with an onset potential as positive as 0.95 ± 0.03 V vs RHE was obtained, and moreover, it showed remarkable stability retaining more than 80% of their initial photocurrent for ≈ 1 h under continuous illumination.[46] This work demonstrated that lead-halide perovskites could indeed be translated into artificial photosynthesis research to realize the ultimate goal of harnessing the power of the sun.
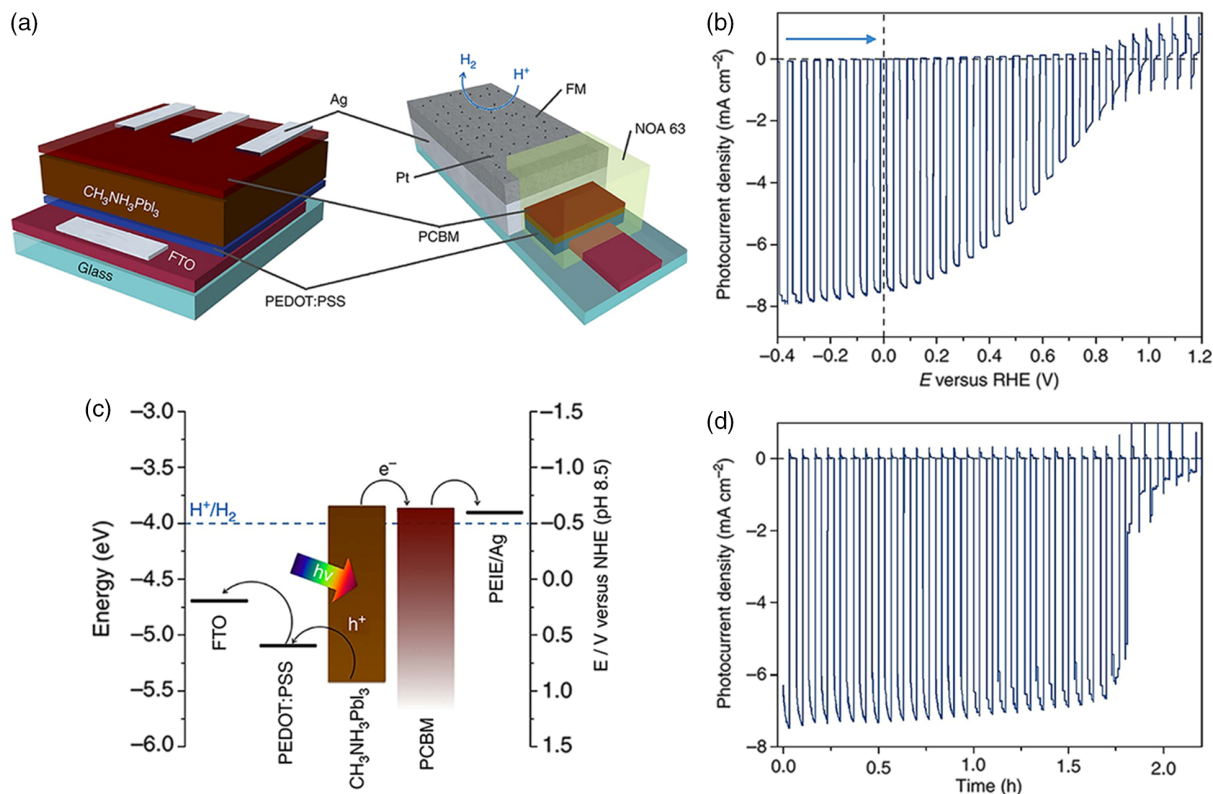
Figure 8. a) Schematic representation of the structure of the perovskite solar cell. An inverted p–i–n configuration was used, with the general FTO/PEDOT:PSS/perovskite/PCBM/PEIE:Ag structure. And Scheme of the solar cell adapted as a photocathode for solar H_2 production. The structure remains the same, but an extra metal-encapsulating layer of FM and Pt as a HEC are added on top of the Ag layer. b) =Typical linear sweep voltammetry of the perovskite-based photocathode at a scan rate of 5 mV s^{-1}. The arrow denotes the scan direction. c) Energy diagram of both devices; for conversion between NHE and RHE reference electrodes, use $E_{RHE} = E_{NHE} + 0.059 \times pH$ and d) Chronoamperometric trace recorded at an applied potential of 0 V vs RHE. An aqueous buffer solution (0.1 M borate, pH 8.5), chopped solar light irradiation (AM 1.5G, 100 mW cm^{-2}, $\lambda > 400$ nm) and an inert (N_2) atmosphere at room temperature were used in both experiments. Reproduced with permission[46] Copyright 2016, Springer Nature.

3.2.2. The Enhancement of Light Absorption

The narrow light absorption region of a photoelectrode is one of the crucial issues that limit the overall efficiency of a PEC device. Generally, coating the core with a shell material may narrow the band gaps, act as an auxiliary light absorber, or reduce light reflection, and thus effectively enhance the overall light absorption. TiO_2 has a high incident photo-to-electron efficiency and a good chemical stability, but its STH efficiency is restricted by the low spectral response characteristic caused by the wide bandgap (≈ 3.2 eV). To narrow the bandgap of TiO_2, Ashai et al. suggested the modification of TiO_2 by different dopants (F, S, N, C or P) on the basis of theoretical calculations.[47b] Yang et al. reported a two-step method to synthesize core-shell nanostructured rutile TiO_2 with S-doped shell and rutile core (R'–TiO_2–S) (**Figure 9**a). Diffuse reflectance spectrum indicated that the band gap of S-doped rutile TiO_2 was significantly reduced to about 1.5 eV (Figure 9d), which is much smaller than that of pristine rutile TiO_2. As a result, the S-doped rutile TiO_2 exhibited an enhanced absorption in visible and NIR regions.[48] In another example, Alotaibi et al. reported a double-band photoelectrode by growing InGaN/GaN core/shell nanowire arrays on Si substrates. The integrated photoanode exhibited a relatively high photocurrent of 23 mA cm^{-2} at 1 V in an acidic solution under AM 1.5G, which was attributed to the narrow band gap (≈ 2.38 eV) of InGaN/GaN core/shell nanowire arrays.[49] In addition, the realization of a highly-stable, scalable, and efficient photoanode in acidic solutions addresses the critical need for PEC water splitting systems. It is also important to notice that such nanowire arrays were grown directly on low cost and large area Si substrate, providing the unique opportunity for integration with Si photocathode for developing high performance and low cost multijunction solar fuel systems.

Another strategy to enhance the light absorption of photoelectrodes is to integrate the wide band gap material with narrow band gap absorbers. For example, Hou et al. prepared vertically aligned ZnO/V_2O_5 core-shell heteronanostructures to broaden the light absorption range of ZnO-based photoanode. With the help of V_2O_5, the photoelectrode showed an enhanced visible light absorption efficiency and a nearly threefold increase in photocurrent density of 1.21 mA cm^{-2} at 1.23 V vs RHE with the electrolyte of 0.5 M Na_2SO_4 (pH ≈ 7.0) and the illuminated light of 100 mW cm^{-2}.[52] In addition, the V_2O_5 cell contributed to the high carrier density, large electrochemically active surface area, carrier density, low charge recombination rate, and the long lifetime of electron-hole pairs due to the formation of the staggered
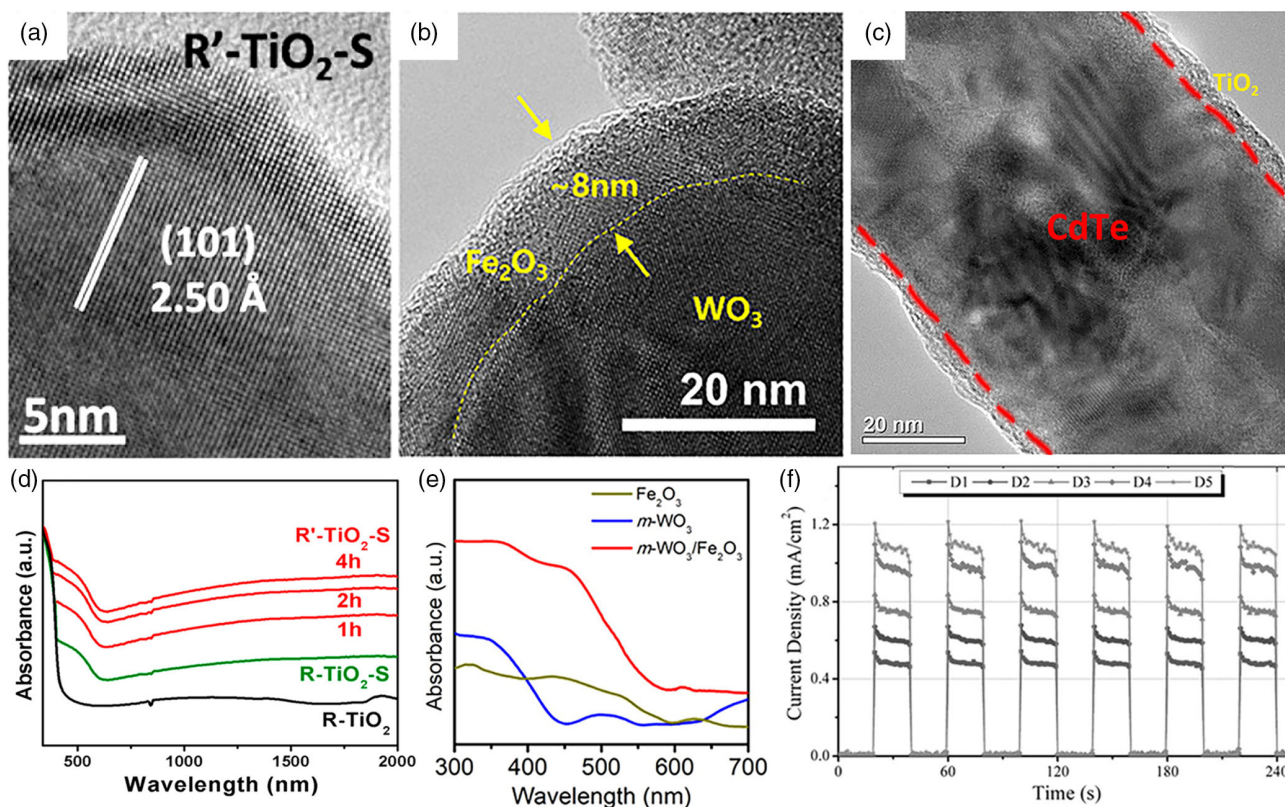
Figure 9. TEM images of core-shell photoanodes. a) R'–TiO$_2$–S, Reproduced with permission.[48] Copyright 2013, American Chemical Society. b) m–WO$_3$/Fe$_2$O$_3$, Reproduced with permission.[50] Copyright 2020, American Chemical Society. and c) CdTe/TiO$_2$. Reproduced with permission.[51] Copyright 2016, WILEY-VCH. Diffuse reflectance spectra of d) R'–TiO$_2$–S, Reproduced with permission.[48] Copyright 2013, American Chemical Society. and e) m–WO$_3$/Fe$_2$O$_3$ photoanodes. Reproduced with permission.[50] Copyright 2020, American Chemical Society. f) Transient photocurrent response of CdTe/TiO$_2$ heteronanostructure arrays with different diameters (D1 = 30 nm, D2 = 45 nm, D3 = 60 nm, D4 = 75 nm, D5 = 90 nm). Reproduced with permission.[51] Copyright 2016, WILEY-VCH.

gap junction. As shown in Figure 9b, Kim et al. fabricated a mesoporous WO$_3$ (m–WO$_3$)/α–Fe$_2$O$_3$ core-shell structured photoanode by an ALD method. Herein, the ultrathin α–Fe$_2$O$_3$ layers acted as a light absorber to extend the light absorption range of the photoanode to the visible range, leading to a high photocurrent density of $\approx$4 mA cm^{-2} at 1.6 V vs RHE under 1 sun illumination of the integrated photoanode (Figure 9e).[50] Similarly, to enhance the visible light response of TiO$_2$, a well-ordered CdTe/TiO$_2$ core/shell nanowire arrays photoelectrode was designed and fabricated by AAO method (Figure 9c).[51] Benefit from the efficient light absorption of CdTe, the CdTe/TiO$_2$ heteronanostructure arrays showed a high photocurrent as 1.1 mA cm^{-2} (Figure 9f), which was much higher than that of a pristine TiO$_2$ electrode.[53]

3.2.3. Introducing a Charge Selective Contact and Improving the Separation and Transport of Charge Carriers

Enhancing the separation and transfer efficiency of photogenerated carriers is of great significance for improving the PEC performance of photoelectrodes. Some research have indicated that coating photoelectrode with certain semiconductors or ferroelectric materials could induce an improved charge

separation and thus effectively improve the transfer efficiency of photo-generated charge carriers.[28b]

According to the semiconductor theory, here, a charge selective contact is generated in the depletion region of the heterojunction consisting of two kinds of semiconductors with matched band structures.[54a] During the past few years, a large variety of heterojunction-type core-shell photoelectrodes had been reported.[55–57] As shown in **Figure 10**a, Huang and coworkers constructed a black BiVO$_4$/TiO$_{2-x}$ core/shell photoelectrode. Due to the heterojunction formed between TiO$_{2-x}$ and black BiVO$_4$ with moderate oxygen vacancies, the solar utilization and the charge transport/separation efficiencies were significantly improved. As a result, BiVO$_4$/TiO$_{2-x}$ exhibited a high photocurrent density of 6.12 mA cm^{-2} at 1.23 V vs RHE for water oxidation and an extraordinary applied bias photon-to-current efficiency of up to 2.5%.[58] Similarly, Si/Ta$_3$N$_5$ core/shell heterojunction photoanodes were designed and fabricated to overcome the charge carriers transport limitations of Ta$_3$N$_5$. It revealed that the incorporation of Ta$_3$N$_5$ on Si enabled a band alignment at the heterojunction. This can remarkably improve the charge extraction and photocurrent onset. Finally, Si/Ta$_3$N$_5$ showed a 10-fold improvement in photocurrent compared to a planar Si/Ta$_3$N$_5$ photoelectrode, and it retained
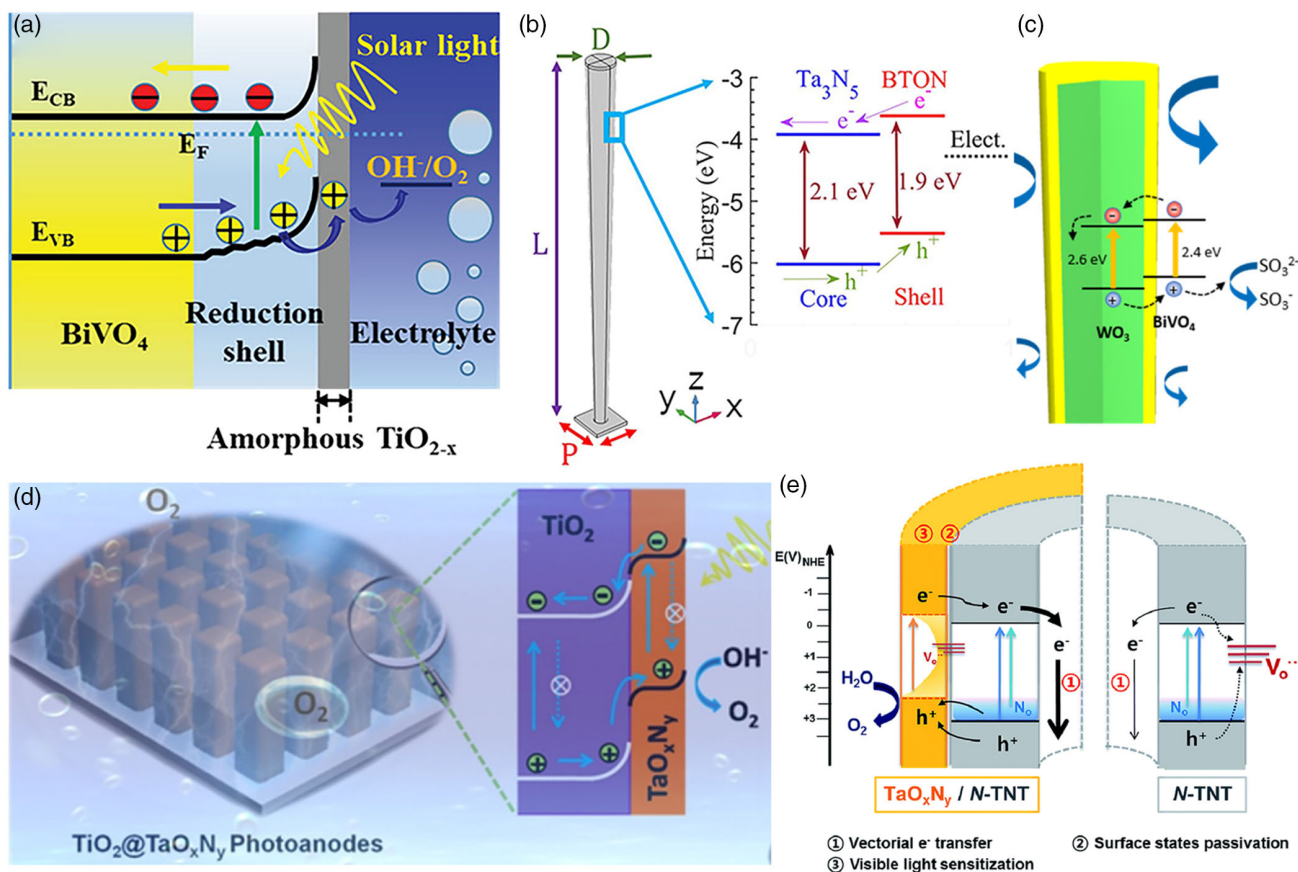
Figure 10. Schematic illustrations of energy band alignment and charge transfer in core/shell photoanodes: a) *b*-BiVO$_4$/TiO$_{2-x}$, Reproduced with permission.[58] Copyright 2019, WILEY-VCH. b) Ta$_3$N$_5$–NR/BTON, Reproduced with permission.[60] Copyright 2020, American Chemical Society. c) WO$_3$/BiVO$_4$, Reproduced with permission.[61] Copyright 2019, American Chemical Society. d) N-doped TiO$_2$ nanotubes (N-TNT) and N-TNT/TaO$_x$N$_y$ hybrid, Reproduced with permission.[62a] Copyright 2019, Elsevier. e) TiO$_2$/Ta$_2$O$_x$N$_y$. Reproduced with permission.[62b] Copyright 2015, The Royal Society of Chemistry.

50–60% of their maximum photocurrent after 24 h chronoamperometry.[22] In another example, Lee et al. prepared a WO$_3$/BiVO$_4$ heterostructure photoanode by an all-solution method.[59] Owing to the appropriate band-edge positions of WO$_3$/BiVO$_4$ heterojunction (Figure 10b), the photocurrent density of the WO$_3$/BiVO$_4$ photoanode reached 4.15 mA cm^{-2} at 1.23 V vs RHE and an IPCE of 75.9% at 430 nm under front illumination.[60] Recently, a core-shell heterojunction of Ta$_3$N$_5$-nanorods/BaTaO$_2$N photoanode was also developed for PEC water splitting.[61] When BaTaO$_2$N was coated on the surface of Ta$_3$N$_5$-nanorods (Figure 10c), a charge selective contact was induced, resulting in efficient generation and separation of charge carriers. Finally, the photocurrent reached up ≈4.5 mA cm^{-2} at 1.23 V$_{RHE}$ under AM 1.5G and stoichiometric O$_2$ and H$_2$, with gas evolution rates of 36.2 and 72.4 µmol h^{-1} cm^{-2}, respectively, were stably produced on the Ta$_3$N$_5$–NRs/BTON/FeNiO$_x$-based photoanode and Pt counter electrode with faradaic efficiencies near 96%. Additionally, the multifunction of Ta$_2$O$_x$N$_y$ shell was confirmed by comparing TiO$_2$/Ta$_2$O$_x$N$_y$ and N-doped TiO$_2$/TaO$_x$N$_y$ core/shell heterojunction photoelectrodes (Figure 10d,e). It showed that Ta$_2$O$_x$N$_y$ could function as both surface sensitizer and charge separator

due to the suitable band structure and the induced charge separating contact.[62] As shown in **Figure 11**, Rao et al. coated W-doped BiVO$_4$ on WO$_3$ nanowires and attained a photocurrent of 3.1 mA cm^{-2} at 1.23 V vs RHE under AM 1.5G, which was more than twice the sum of the separate photocurrents of the bare WO$_3$ nanowire array and a "same-mass W:BiVO$_4$ film".[63] Such high photocurrent was attributed to the powerful synergistic effect between the WO$_3$ core and the W:BiVO$_4$ shell, and this synergy was also evident in the corresponding performance enhancement in the IPCE results.

Another representative strategy to promote the separation and transport of charge carriers in core/shell photoelectrodes is to coat the photoelectrode with a layer of ferroelectric materials. Specifically, the centers of positive and negative charges are not symmetrical in ferroelectric materials, which could polarize a large, stable and tunable remanent ferroelectric polarization by an external potential, resulting a charge separation extending over the whole film volume, whereby giving the photoelectrode high efficiency in separating charge carriers and switching charge-transfer directions. In the past decades, ferroelectric materials, such as BiFeO$_3$ (BFO), Pb(Zr,Ti)O$_3$ (PZT), and SrTiO$_3$ (STO), have been widely used in the construction
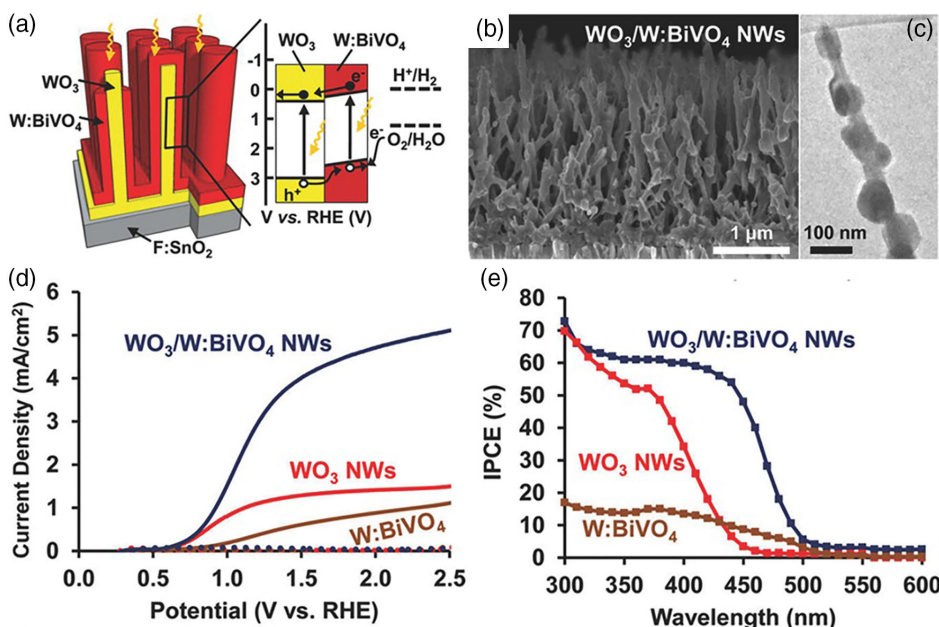
Figure 11. a) Structural schematic and energy band diagram of the core/shell NWs and type-II staggered heterojunction, in which charges generated in both the $W:BiVO_4$ shells and WO_3 NW cores can contribute to the water oxidation photocurrent. b,c) SEM and TEM images of $WO_3/W:BiVO_4$ hybrid nanowires. d) J–V curves of the $WO_3/W:BiVO_4$ NW photoanode and control samples measure under AM 1.5G illumination in 0.5 M potassium phosphate electrolyte buffered to pH of 8. e) IPCE curves measured at 1.23 V vs RHE. Reproduced with permission.[63] Copyright 2017, WILEY-VCH.

of photoelectrodes for PEC water spitting in the form of ITO/nano-Au/PZT and BFO/CdSe heterostructures, etc.[64,65] As shown in **Figure 12**a,b, Yang et al. have synthesized a

$TiO_2/BaTiO_3$ core/shell nanowires (NWs) by a hydrothermal process. Compared with the pristine TiO_2, the $TiO_2/BaTiO_3$ photoanode exhibited 67% improvement in photocurrent density
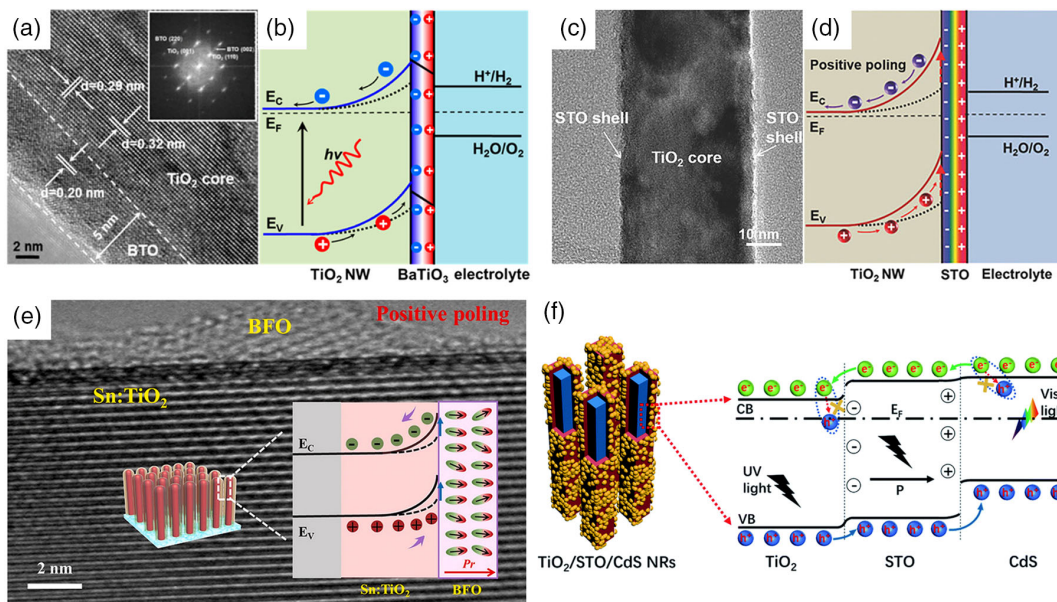
Figure 12. TEM images of core/shell NWs: a) TiO_2/BTO NW, Reproduced with permission.[66] Copyright 2015, American Chemical Society. c) TiO_2/STO, Reproduced with permission.[64a] Copyright 2017, WILEY-VCH. e) $BFO/Sn:TiO_2$.[67a] Schematic diagrams of the enhancing effect of the polar charge-induced selectivity for the separation of photo-induced charge carriers for b) TiO_2/BTO, Reproduced with permission.[66] Copyright 2015, American Chemical Society. d) TiO_2/STO, Reproduced with permission.[64a] Copyright 2017, WILEY-VCH. and e) $BFO/Sn:TiO_2$ core/shell NW photoelectrodes. Reproduced with permission.[67a] Copyright 2019, Elsevier. f) Dual-regulation charges separation strategy of the $TiO_2/STO/CdS$ NRs photoelectrode. Reproduced with permission.[67b] Copyright 2021, The Royal Society of Chemistry.

from 0.78 to 1.30 mA cm^{-2} due to the remarkably increased charge separation efficiency induced by the ferroelectric polarization of the BaTiO$_3$ (BTO) shell. Especially, the increase or decrease of photocurrent could be switched by the direction of the ferroelectric polarization induced by the charge selectivity.[66] Similarly, a TiO$_2$/STO core/shell NWs was prepared (Figure 12c,d). The experimental results indicated that the electrical band bending of TiO$_2$ could be effectively regulated by ferroelectric polarization generated in STO shell, resulting in significantly enhancement of the charge separation.[64a] Additionally, BFO/Sn:TiO$_2$ (Figure 12e) and TiO$_2$/STO/CdS (nanorod/ferroelectric/quantum dot) dual modification composite photoanodes (Figure 12f) were constructed, respectively. Benefit from polar charge-induced selectivity, the dual regulation in core/shell photoelectrodes showed persistent and rapid charge separation and transport both in bulk and photoelectrode interfaces.[67]

3.2.4. The Improvement of Surface Reactions

Generally, the slow water redox kinetics may originate from two major reasons. First, it might be ascribed to the facile recombination of charge carriers before transporting to the catalytic active sites on the surface of photoelectrodes. Second, the sluggish surface reactions, particularly for the oxygen evolution reaction, could cause the consumption of charge carriers.[68] Representative strategies in addressing the above two issues are to coat or load cocatalysts on the surface of photoelectrode, which may introduce new energy level and lower the activation energy, thus to facilitate surface reaction and improve the stability of photoelectrodes. Moreover, the cocatalyst can serve as trapping sites for photo-generated charge carriers and enhancing the separation and transport of charge carriers.[69]

Precious metals (e.g., Pt[70]) and transition metal based catalysts (e.g., MoS$_2$,[71] MoSe$_2$,[15a,72] CoP,[73] or pseudomolecular MNC[74]) have been widely used for the hydrogen evolution reaction (HER). MoS$_2$ is a low-cost and scalable crystalline catalyst for HER. Recently, Guo and coworkers prepared core/shell Sb$_2$Se$_3$/MoS$_2$ nanorod (NR) arrays photocathode by sputtering MoS$_2$ as a HER catalyst on the high quality Sb$_2$Se$_3$ NR arrays. It showed that the thin MoS$_2$ shell and Sb$_2$Se$_3$ formed a suitable band alignment, which could not only prevent the photoelectrode from corrosion but also promote the carrier transport. Consequently, the PEC activity of MoS$_2$/Sb$_2$Se$_3$ photocathode was increased with a photocurrent as high as -10 mA cm^{-2} at 0 V vs RHE under a simulated AM 1.5 solar illumination, and an IPCE as high as 33% at 800 nm.[71b]

In the case of oxygen evolution reaction (OER), various catalysts including precious metal (e.g., Ru and Ir), transition metals (e.g., Co, Ni, and Fe) oxides and (oxy)hydroxides have been widely applied to enhance surface OER by reducing the reaction energy.[15b,15c,32a,75] Generally, these materials could either take over the catalytic function, provide photovoltage or contribute to both aspects. One group of representative cocatalysts for core/shell photoelectrodes are Fe-based electrocatalysts. For instance, Li et al. prepared a Fe$_2$O$_3$/NiFe(OH)$_x$ core/shell photocathode using a citrate-assisted method by coating Fe$_2$O$_3$ with Ni-Fe hydroxide (NiFe(OH)$_x$), as shown in **Figure 13**a,b. The experimental results demonstrated that NiFe(OH)$_x$ overlayers not only

facilitate the hole transport but also passivate the surface states of Fe$_2$O$_3$, and endow the integrated photoanode with a low early onset potential of 0.53 V vs RHE, a photocurrent of 0.55 mA cm^{-2} at 1.23 V vs RHE, the 95% of the initial value of the photocurrent after testing for 7 h under light illumination, and the Faradic efficiencies of oxygen and hydrogen of 92.5% and 90.2%, respectively.[15c] Moreover, in order to build highly-matched semiconductor/cocatalyst interface, Chen et al. coated Fe$_2$O$_3$ with NiFeOOH layer by a simple electroless ligand-regulated oxidation method (Figure 13c). The NiFeOOH overlayers could enhance the OER kinetics and lower the overpotential of the prepared photoanodes. As a result, in comparison with bare Fe$_2$O$_3$, semi-FeOOH and NiOOH decorated Fe$_2$O$_3$ photoanodes, the Fe2O3/NiFeOOH core-shell photoanodes exhibited obviously enhanced photocurrent density (1.83 mA cm^{-2} at 1.23 V vs RHE) and stability.[15b] Furthermore, a Fe$_2$O$_3$/Fe-based MOF core/shell photoanode was constructed by a facile surfactant-assisted solvothermal method (Figure 13c), where the charge carrier separation and hole injection efficiency were significantly promoted due to the cascade band level and more active sites provided by the Fe-based MOF shell with the photocurrent density of 2.27 mA cm^{-2} at 1.23 V vs RHE.[15d] In addition, the amino group functionalized ligand of NH$_2$-MIL-101(Fe) is found to be beneficial to both the light absorption and the stabilization of the photoexcited state.

Cobalt (oxy)hydroxides are another type of cocatalysts for core/shell photoanodes.[32a,76] Li et al. synthesized a wormlike nano-structured hematite (WN–α–Fe$_2$O$_3$)@Co$_3$O$_4$ core/shell nanoarray photoanode through an in-situ hydrothermal growth followed by calcination strategy. Due to the remarkable enhancement of charge carrier separation and transport as well as OER kinetics originating from the Co$_3$O$_4$ shells, the as-prepared photoanode showed a significantly improved OER activity with a photoconversion efficiency of 0.55%, which was about 4 times higher than that of WN–α–Fe$_2$O$_3$ (0.14%), and a photocurrent density of 3.48 mA cm^{-2} at 1.23 V vs RHE.[76] This work not only presents a novel low-cost and earth-abundant WN–α–Fe$_2$O$_3$@Co$_3$O$_4$ photoelectrode with superior PEC water oxidation performance, but also offers a general strategy for the in situ growth of water oxidation catalysts on various photoelectrodes with 3D complex geometries for PEC water splitting. Similarly, a Co(OH)$_x$ encapsulated p–Cu$_2$S/n–BiVO$_4$ photoanode was prepared (**Figure 14**a–c), and it was found that Co(OH)$_x$ coating could simultaneously improve charge separation and surface reaction kinetics in PEC water splitting, where the photocurrent density reached up to 3.51 mA cm^{-2} at 1.23 V$_{RHE}$ and the ABPE was of 0.94% at 0.74 V$_{RHE}$.[77] Recently, many Co-based core/shell photoelectrodes were developed to resolve the issue of catalytic activity and stability at the same time.[78] As shown in Figures 13d,e, Chen et al. prepared a photoanode with a dual co-catalyst shell, where a continuous CoPi layer with many non-continuous Co(OH)$_2$ islands on its top was coated on the surface of Ta$_3$N$_5$ nanorods. The shell could not only prevent the Ta$_3$N$_5$ from self-oxidation, but also facilitate charge carrier separation, thereby the as-synthesized photoanode exhibited significantly enhanced PEC water splitting performance and stability compared with CoPi–Ta$_3$N$_5$ and Co(OH)$_2$–Ta$_3$N$_5$ photoanodes, where the photocurrent density of CoPi/Co(OH)$_2$–Ta$_3$N$_5$ reached up to $\approx$3.8 mA cm^{-2} at 1.23 V vs RHE, and over 90%
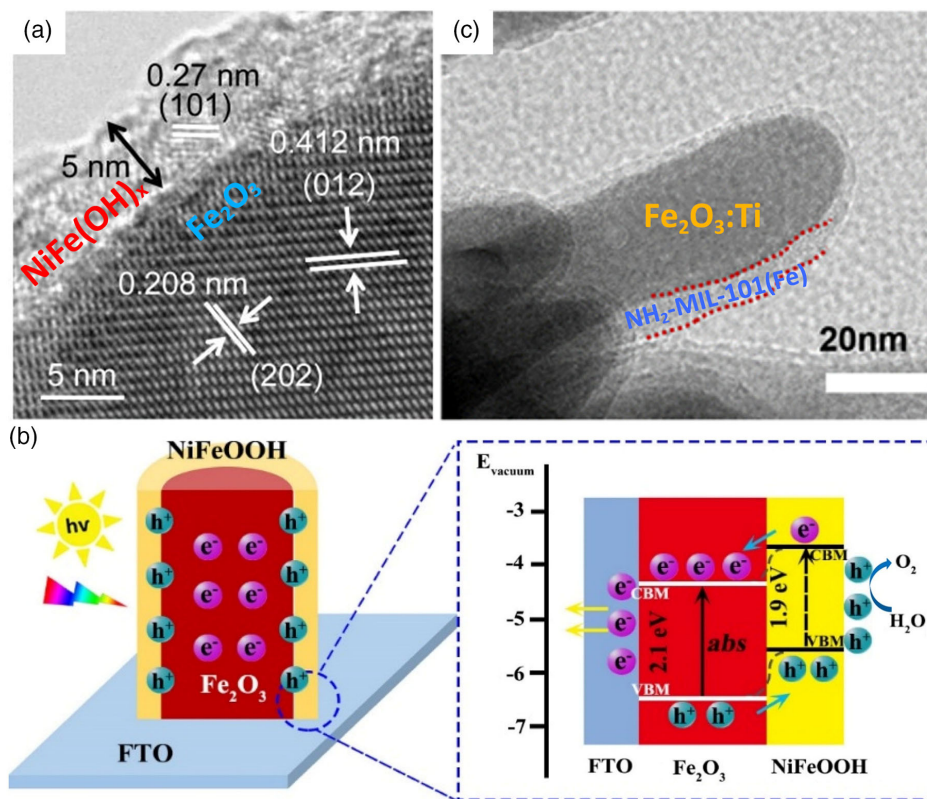
Figure 13. TEM images of Ni-Fe hydroxide coated hematite NW a), Reproduced with permission.[15c] Copyright 2019, American Chemical Society. and Fe$_2$O$_3$:Ti/NH$_2$-MIL-101(Fe) c), Reproduced with permission.[15d] Copyright 2018, Elsevier. b) Schematic illustration of the band alignment of the Fe$_2$O$_3$/NiFeOOH core/shell NAs. Reproduced with permission.[15b] Copyright 2020, Elsevier.

of the initial value could be retained after a 20 min stability test duration.[78a] The strategy shown here might be applicable to enhance the PEC performance of other light absorbers with wide absorption range but low resistance to self-oxidation. Moreover, Wu et al. revealed that Co(CO$_3$)$_x$OH$_y$ on BiVO$_4$ showed the best cocatalyst and protector effects for the first time (Figure 14f). Interestingly, the Co(CO$_3$)$_x$OH$_y$ also exhibited a good self-healing function in borate buffered electrolyte.[79]

The comparison of various properties, including synthesis method, band gaps of light absorbers, and performance, for each system of the core-cell tandem nanostructures is listed as **Table 1**.

4. Two-Photoelectrode Tandem Cell

Configuring a two-photoelectrode tandem PEC cell is considered to be an inspiring way to segment the required potential for water splitting (at least 1.6 V) in operation and combine different band alignments for efficient light absorption and unassisted overall water splitting.[80] The two photoelectrodes provide about 0.7 and 1.0 V separately and could be composed of a wide variety of semiconductors with narrow or wide band gaps. This multiphoton-absorption tandem device increases the overall cell efficiency since it utilizes a wide range of the solar spectrum to generate sufficient driving photovoltages needed for water splitting while simultaneously maximizing the fraction of solar

energy collected.[81] It is prejudged that a two-photoelectrode tandem cell can reach an efficiency of >20% in theory.[82] The materials selection of photoanode and photocathode mainly considers the band structure and n– or p–type of semiconductors. In a general way, the band bending of the p–type semiconductors at the interface with the electrolyte favors water reduction (H$_2$ generation) as a photocathode, while n–type semiconductors are appropriate for photoanodes. After the photovoltage satisfies the minimum requirements (1.6 V, see above), the PEC water splitting efficiency is directly determined by the photocurrent generated from the photoelectrodes. The correct alignment of the conduction band (CB) and valence band (VB) positions; respectively, of the photoanode and -cathode is a pre-requirement; however, the overlab should be small as it would otherwise result in low efficiency. Si, III–V semiconductors, Cu$_2$O, TiO$_2$, Fe$_2$O$_3$, BiVO$_4$, and other oxides have been demonstrated to be potential ingredients for an efficient tandem PEC device.[83] The two-photoelectrode tandem cell can be classified in monolithic- and parallel-type.

4.1. Two-Photoelectrode Tandem Cell in Monolithic Devices

In a monolithic PEC device, the photoanode and photocathode are series attached at the two sides of the monolithic device, allowing to achieve minimized electrodes distance and improved redox reaction efficiency. This design also reduces the occupation
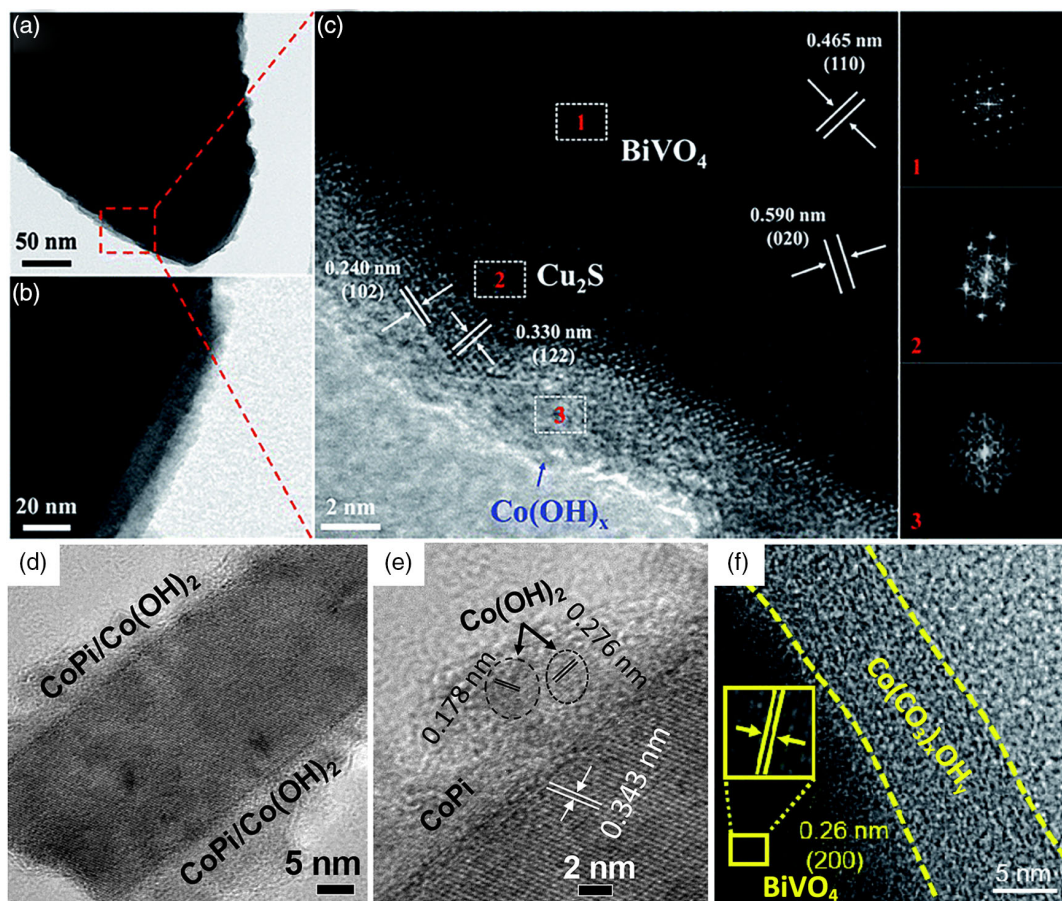
Figure 14. TEM images a,b) and c) HRTEM images with selected area electron diffraction patterns for Co(OH)$_x$ encapsulated p–Cu$_2$S/nBiVO$_4$ photoanode. Reproduced with permission.[77] Copyright 2019, The Royal Society of Chemistry. d) TEM and e) HRTEM images of CoPi/Co(OH)$_2$–Ta$_3$N$_5$ films. Reproduced with permission.[78a] Copyright 2019, Elsevier. f) TEM images of BiVO$_4$/Co(CO$_3$)$_x$OH$_y$ photoanode. Reproduced with permission.[79] Copyright 2020, The Royal Society of Chemistry.

of space and provides a configuration basis for the reasonable utilization of incident light. TiO$_2$ nanorod arrays have been selected to construct a double-sided tandem photoelectrode, where TiO$_2$ nanorod arrays grow on both sides of the conductive transparent substrate by hydrothermal method, and then CdS quantum dots (QDs) and CdSe QDs were coated on TiO$_2$ at two sides, respectively (**Figure 15**a).[84] CdS and CdSe QDs were both absorbers for visible light, and they injected electrons to the CB of TiO$_2$. This tandem photoelectrode exhibited a STH efficiency of 2.78%, attributing to the pronounced enhancement in light-harvesting. Similarly, double-sided CdS and CdSe QDs co-sensitized ZnO nanowire arrays photoelectrode has been constructed for PEC H$_2$ generation. It exhibited a strong absorption in nearly the entire visible spectrum reached up to 650 nm, and the IPCE and photocurrent density were ≈45% at 0 V vs Ag/AgCl and ≈12 mA cm^{-2} at 0.4 V vs Ag/AgCl, respectively.[85] A dual-junction tandem photoelectrode was designed and demonstrated with increased PEC water splitting photocurrent.[86] In this monolithic PEC device, GaInP and GaInAs subcells were grown via metal organic vapor phase epitaxy on a GaAs substrate, and a crystalline TiO$_2$ layer (anatase structure) served as

protective layers on the cathode, as shown in Figure 15b. A layer of Rh nanoparticles and a sputtered RuO$_2$ film served as HER and OER catalysts, respectively. Rh nanoparticles were properly designed in size distribution and spatial arrangement to achieve ultralow light attenuation. The TiO$_2$ layer not only restrained corrosion but also facilitated the electron transport at the cathode-electrolyte interface thanks to its favorable band alignment between its CB and the thermodynamic potential for water reduction. This complex but elaborate design allowed the tandem PEC device to achieve the STH efficiency of 19.3% in an acidic electrolyte and a STH efficiency of 18.5% in a neutral electrolyte, which reached the value of 0.85 of the theoretical limit for PEC water splitting for the energy gap combination employed in the tandem-junction photoelectrode structure. Ahmet et al. fabricated a planar and nanostructured n–Si/SiO$_x$/TiO$_2$/WO$_3$/BiVO$_4$ monolithic core/shell photoanode using chemical deposition methods,[87] where SnO$_2$ and TiO$_2$ planar thin films were formed by aerosol-assisted chemical vapor deposition while WO$_3$ nanorods grew perpendicular onto the films and BiVO$_4$ was coated subsequently on WO$_3$ via solution deposition to form a core-shell structure. A layer of Fe(Ni)OOH was deposited to

Table 1. The synthesis method and performance for each system of the core-cell tandem nanostructures.

The composition of nanostructure	Synthetic method	Band gaps of light absorbers	Performance	References
CdS/ZnS core-shell (CS) nanorod array (NDA) photoanode	aerosol assisted chemical vapor deposition (AACVD)	2.4 eV for CdS	7.8 mA cm^{-2} (0 V vs SCE), 100 mW cm^{-2}, AM 1.5G, 0.25 mol L^{-1} Na$_2$S + 0.35 mol L^{-1} Na$_2$SO$_3$. IPCE above 35% at 0 V vs SCE under 300 nm. The stability of over 16 min.	[33]
Pt/TiO$_2$/Bilayer Sb$_2$Se$_3$/Au/FTO ND photocathode	Sequential use of two different molecular inks	3.2 eV for anatase, 3.0 eV for rutile; 1.15 eV for Sb$_2$Se$_3$	30 mA cm^{-2} at 0 V vs RHE, under pH 1, H$_2$SO$_4$ electrolyte. IPCE of 85.7% at 0 V vs RHE under 750 nm. Maintaining nearly 100% of the initial photocurrent after 5 h of operation in a pH 1 solution and 85% after 10 h of operation in a pH 6.5 solution. The Faradaic efficiency of the H$_2$ evolution >90% in the pH 1 electrolyte.	[37]
Pt/C$_{60\ pat.}$-TiO$_2$ ball/GeSe CS photocathode	Thermal sublimation deposition method, sol-gel method, photodeposition method	3.2 eV for anatase, 3.0 eV for rutile; 1.2 eV for GeSe	Long-term stability of 60 h for the single photocathode. Photocurrent onset (0.6 V$_{RHE}$). STH of 1.37% with stability over 12 h of a GeSe–BiVO$_4$ tandem cell for unbiased overall solar water splitting.	[38]
Si/ITO–Au/Cu$_2$O/ZnO/TiO$_2$/Pt Micropillar Array photocathode	Pulsed laser deposition (PLD)	1.1 eV for Si; 2.1 eV for Cu$_2$O; 3.2 eV for ZnO; 3.2 eV for anatase, 3.0 eV for rutile	7.5 mA cm^{-2} at 0 V vs RHE and an onset potential of 0.85 V vs RHE, with a stable operation for 75 h.	[14]
CS TiO$_2$@Au$_{25}$/TiO$_2$ nanowire arrays (NWA) photoanode	atomic layer deposition (ALD)	3.2 eV for anatase, 3.0 eV for rutile	1.35 mA cm^{-2} at 1.23 V vs RHE. Stability over 4 h at 1.23 V vs RHE The generation rate of 35.88 µmol h^{-1} for H$_2$ and 18.06 µmol h^{-1} for O$_2$. The FE of H$_2$ and O$_2$ is ≈92 and ≈93%.	[43]
Co–Pi decorated g–C$_3$N$_4$@ZnO CS NDA photoanode	Urea impregnation and calcination method	2.7 eV for C$_3$N$_4$; 3.2 eV for ZnO	Photocurrent of 5 mA cm^{-2} under the bias of 1.23 V vs RHE.	[45]
InGaN/GaN CS NW photoanode	Catalyst-free molecular bean epitaxy	3.51 eV for GaN	IPCE ≈27% at 350 nm and 1 V vs Ag/AgCl. Photocurrent of 23 mA cm^{-2} at 1 V vs Ag/AgCl, under AM 1.5G.	[49]
ZnO/V$_2$O$_5$ CS ND photoanode	Hydrothermal growing and radio frequency (RF) magnetron sputtering deposition	3.2 eV for ZnO; 2.32 eV for V$_2$O$_5$	1.21 mA cm^{-2} at 1.23 V vs RHE in 0.5 M Na$_2$SO$_4$ and 100 mW cm^{-2} with AM 1.5G IPCE of 82.3%.	[52]
WO$_3$–Fe$_2$O$_3$–TiO$_2$–CoPi layered photoanode	Drop-casting method ALD	2.7 eV for WO$_3$; 2.1 eV for Fe$_2$O$_3$; 3.2 eV for anatase, 3.0 eV for rutile	≈4 mA cm^{-2} photocurrent density at 1.6 V vs RHE under 1 sun illumination.	[50]
CdTe/TiO$_2$ CS NWA photoanode	convenient AAO template method	1.37–1.54 eV for CdTe; 3.2 eV for anatase, 3.0 eV for rutile	Photocurrent of 1.16 mA cm^{-2} at 1.12 V vs RHE (AM 1.5G, 100 mW cm^{-2}, 1 M NaOH) Photoconversion efficiency (η) of 0.85% at 0.09 V vs RHE.	[51]
Si–Ta$_3$N$_5$ CS photoanode	ALD	1.1 eV for Si; 2.0 eV for Ta$_3$N$_5$	Retained 50–60% of their maximum photocurrent after 24 h chronoamperometry experiments.	[22]
WO$_3$/BiVO$_4$ CS NDA photoanode	Hydrothermal method and pulsed electrodeposition	2.7 eV for WO$_3$; 2.4 eV for BiVO$_4$	4.15 mA cm^{-2} at 1.23 V vs RHE. IPCE of 75.9% at 430 nm under front illumination.	[60]
Ta$_3$N$_5$/BaTaO$_2$N CS ND photoanode	Glancing angle deposition and dip coating technique	2.0 eV for Ta$_3$N$_5$; 1.8–1.9 eV for BaTaO$_2$N	≈4.5 mA cm^{-2} at 1.23 V$_{RHE}$ under AM 1.5G. The stoichiometric evolution of O$_2$ and H$_2$ of 36.2 and 72.4 µmol h^{-1} cm^{-2}, respectively, from water occurs steadily over an hour with faradaic efficiencies of 90%−95%	[61]

Table 1. Continued.

The composition of nanostructure	Synthetic method	Band gaps of light absorbers	Performance	References
Amorphous $Ta_2O_xN_y$ enwrapped TiO_2 rutile CS ND photoanode	Hydrothermal, Solution Dropping, Calcination, and Ammonization	2.95 eV for $Ta_2O_xN_y$; 3.2 eV for anatase, 3.0 eV for rutile	IPCE of 22.6% in a two-electrode system under 390 nm. Photocurrent density of 1.32 mA cm^{-2} at 1.23 V vs RHE. The oxygen evolution rate of 112.7 mmol m^{-2} h^{-1}. A solar-to-chemical energy conversion efficiency of 1.49% at 1.23 V vs RHE.	[62a]
TiO_2/$BaTiO_3$ CS NW photoanode	A one-step hydrothermal method	3.2 eV for anatase, 3.0 eV for rutile; 3.2 eV for $BaTiO_3$	Photocurrent of 1.30 mA cm^{-2} at 1.23 V vs RHE.	[66]
TiO_2–$SrTiO_3$ CS NW Photoanode	Hydrothermal method	3.2 eV for anatase, 3.0 eV for rutile; 3.25 eV for $SrTiO_3$	J_{ph} and $\eta_{separation}$ of 1.43 mA cm^{-2} and 87.7% at 1.23 V vs RHE, respectively.	[64a]
MoS_2/Sb_2Se_3 CS NDA photocathode	Sputtering Deposition	1.96 eV for MoS_2, 1.1 eV for Sb_2Se_3	Photocurrent density of −10 mA cm^{-2} at 0 V$_{RHE}$ in a buffered near-neutral solution (pH 6.5) under AM 1.5G. An IPCE as high as 33% at 800 nm.	[71b]
Fe_2O_3/citrate/$NiFe(OH)_x$ CS NWA photoanode	Citrate-assisted method	2.1 eV for Fe_2O_3	An early turn-on potential of 0.53 V vs RHE. The photocurrent of 0.55 mA cm^{-2} at 1.23 V vs RHE. Retained 95% of the photocurrent after testing for 7 h under light illumination. The Faradaic efficiencies of oxygen and hydrogen were 92.5 and 90.2%, respectively.	[15c]
Fe_2O_3–NiFeOOH CS NDA photoanode	Electroless ligand-regulated oxidation method	2.1 eV for Fe_2O_3	The photocurrent density of 1.83 mA cm^{-2} at 1.23 V$_{RHE}$. A ≈10% decay of photocurrent under illumination for 2 h. Applied bias photon-to-current efficiency (ABPE) of 0.22% at 1.0 V$_{RHE}$. IPCE of 40.7% at 410 nm	[15b]
Fe_2O_3/Fe-based MOF CS ND photoelectrode	A surfactant-assisted solvothermal method	2.1 eV for Fe_2O_3	Photocurrent density of 2.27 mA cm^{-2} at 1.23 V vs RHE. IPCE of 42.3% at 365 nm with an applied external potential of 1.23 V vs RHE	[15d]
Wormlike nanostructured hematite (WN–α–Fe_2O_3) @Co_3O_4 CS NA photoanode	in situ hydrothermal growth followed by calcination strategy	2.1 eV for Fe_2O_3; 1.21 eV for p–Cu_2S; 2.4 eV for $BiVO_4$	Photocurrent density of 3.48 mA cm^{-2} at 1.23 V vs RHE. Photoconversion efficiency of 0.55%.	[76]
$Co(OH)_x$ encapsulated p–Cu_2S n$BiVO_4$ CS photoanode	Successive ion layer adsorption and reaction (SILAR)		Photocurrent density of 3.51 mA cm^{-2} at 1.23 V vs RHE. ABPE of 0.94% at 0.74 V$_{RHE}$.	[77]
CoPi/$Co(OH)_2$–Ta_3N_5 NDA photoanodes	Hydrothermal method, SILAR, photo-assisted electrodeposition process	2.0 eV for Ta_3N_5	The photocurrent density of ≈3.8 mA cm^{-2} at 1.23 V vs RHE, Over 90% of the initial value of photocurrent were retained after a 20 min stability test.	[78a]

optimize the hybrid photoanode, and the optimized photoanode was combined with a Pt cathode for unassisted solar water splitting. A maximum photocurrent density of 0.3 mA cm^{-2}, with a STH of 0.37%, was observed in this tandem PEC cell. The electrolyte was a film-shaped solid electrolyte, and the two photoelectrodes were located on both sides of the membrane. Based on this idea, another kind of monolithic two-electrodes tandem system was designed. Two kinds of monolithic solid-state PEC devices were prepared and compared for water alleviating in the gas phase, one Pt-based cathode (n–type|Nafion|C-Pt) and another g/C_3N_4–based tandem cell (n–type|Nafion|p–type).[88]

Solidified Nafion was selected as the separated membrane and adhesive. Both of them utilized mesh TiO_2 nanotubes as photoanode. For the PEC tests, the photoanode was supplied with wet air of relative humidity of 80%, while the photocathode was supplied with dry Ar. The protons generated from the water oxidation directly entered the polymer electrolyte since the reaction occurred at the triple-phase boundary. The g/C_3N_4-based tandem configuration exhibited a three-fold enhancement in the open-circuit voltage compared to Pt-based cell, and it showed longtime stability and significant improvement in photocurrent density. For this tandem n-type|Nafion|p–type system, the two type
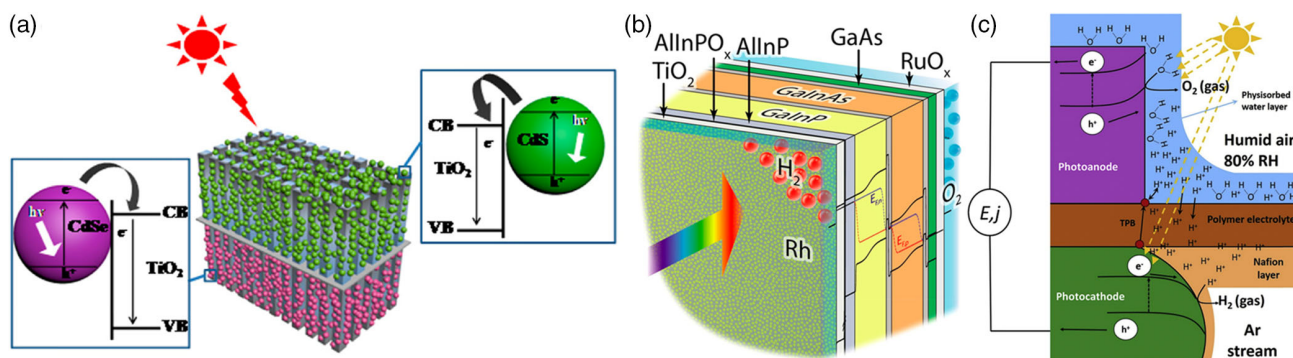
Figure 15. a) Illustration of CdS/CdSe QDs co-sensitized TiO_2 nanorod arrays tandem PEC structure. Reproduced with permission.[84] Copyright 2016, American Chemical Society. b) Schematic of the monolithic $Rh/TiO_2/III–V$ semiconductors/RuO_x tandem as record PEC device for unassisted water splitting. Reproduced with permission.[86] Copyright 2018, American Chemical Society. c) Illustration of the n–type|Nafion|p–type tandem configuration and its water vapor splitting process. Reproduced with permission.[88] Copyright 2019, Elsevier.

semiconductors increased the internal voltage of the device, and the proton reduction by g/C_3N_4 was thermodynamically favorable. The concept of solar water vapor splitting and the structure of this tandem PEC device can be seen in Figure 15c, where the system was based on earth-abundant materials and provided a way of artificial photosynthesis for areas where water sources were scarce and electrical grid infrastructure was limited.

In conclusion, the monolithic two-photoelectrodes tandem PEC cells are generally fabricated in two ways: first, growing light absorbers on both sides of a conductive substrate with a double-sided conductive film; second, the polymer film with certain supporting strength is used as the intermediate layer, and photoanode and photocathode are grown on the opposite sides of this membrane. In this case, the membrane contained is required to have certain conductivity, supportability, and relatively thin thickness.[89] A crucial point for such configurations will also be to avoid swelling and shrinking of the membrane by varying humidity in the environment. This would impact the ion conductivity and the adhesion of the photoelectrode layers. The simple models of these two kinds of monolithic tandem structures are given in **Figure 16**.

4.2. Two-Photoelectrode in Parallel Tandem Cell

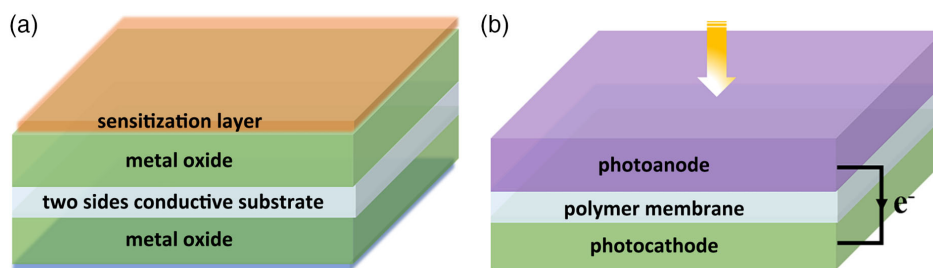Two photoelectrodes in parallel tandem PEC cell refers to the device in which the photoanode and photocathode are on different monolithic electrodes and connected by a wire (**Figure 17**). Photons with shorter wavelengths of the solar spectrum are first absorbed by one photoelectrode, and the remaining photons will be captured by another photoelectrode.[83]
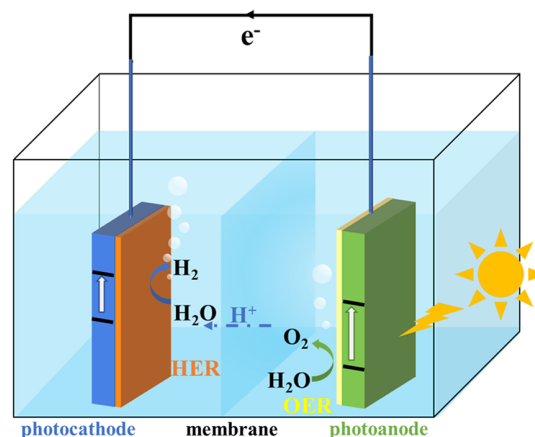
Figure 17. Simple schematic representation of two-photoelectrodes in parallel tandem PEC device for unassisted water splitting. HER and OER catalysts are coated on the main materials, while other protection or optimization layered structures are not displayed in the schematic. The separated membrane is used to avoid the mixing of prepared H_2 and O_2 gases.

Figure 16. Diagram of the three typical kinds of monolithic two-photoelectrodes tandem PEC device. a) Double-sided metal oxide growth on one conductive substrate with both sides sensitized. b) A tandem PEC cell that photocathode and photoanode grow on the opposite sides of the separated membrane.

Optimizing the photoanode and/or photocathode and utilizing a universal counter electrode is a common exploring mode in this parallel dual-electrode system. After selecting the semiconductors with suitable band structures as the photoanode or photocathode, various strategies have been applied to further optimize the PEC performance of the entire device, including sensitization, constructing multi-layer heterostructure, and the addition of protected layer for high stability, etc. Sensitization has been applied to construct high-efficient PEC tandem cells. Sen et al. used an organic dye L0 as a photosensitizer for a mesoporous TiO_2 based photoanode and an organic dye P1 as light-absorber for a nano NiO-based photocathode. As shown in **Figure 18**a, a molecular complex Ru1 and Co1 were selected as water oxidation catalyst and

hydrogen generation catalyst, respectively.[90] The band alignment of these materials was as much optimized that it boosted the efficient charge transfer and visible-light-driven redox reactions. This work provided the first example of a metal-free, organic dye-sensitized tandem PEC cell with a photocurrent density of $300\,\mu A\,cm^{-2}$ and an IPCE of 25% at 380 nm under neutral pH conditions without applying any bias. Cui et al. also represented a zeolitic-imidazolate-framework-67 (ZIF-67) sensitized WO_3 photoanode, and they paired it with a Z-scheme $BiVO_4$/black phosphorus (BP) photocathode to configure a tandem PEC cell.[91] The deliberate design for band alignment between two photoelectrodes allowed a reversible electron storage property and enabled light-generated charge storing and on-demand release
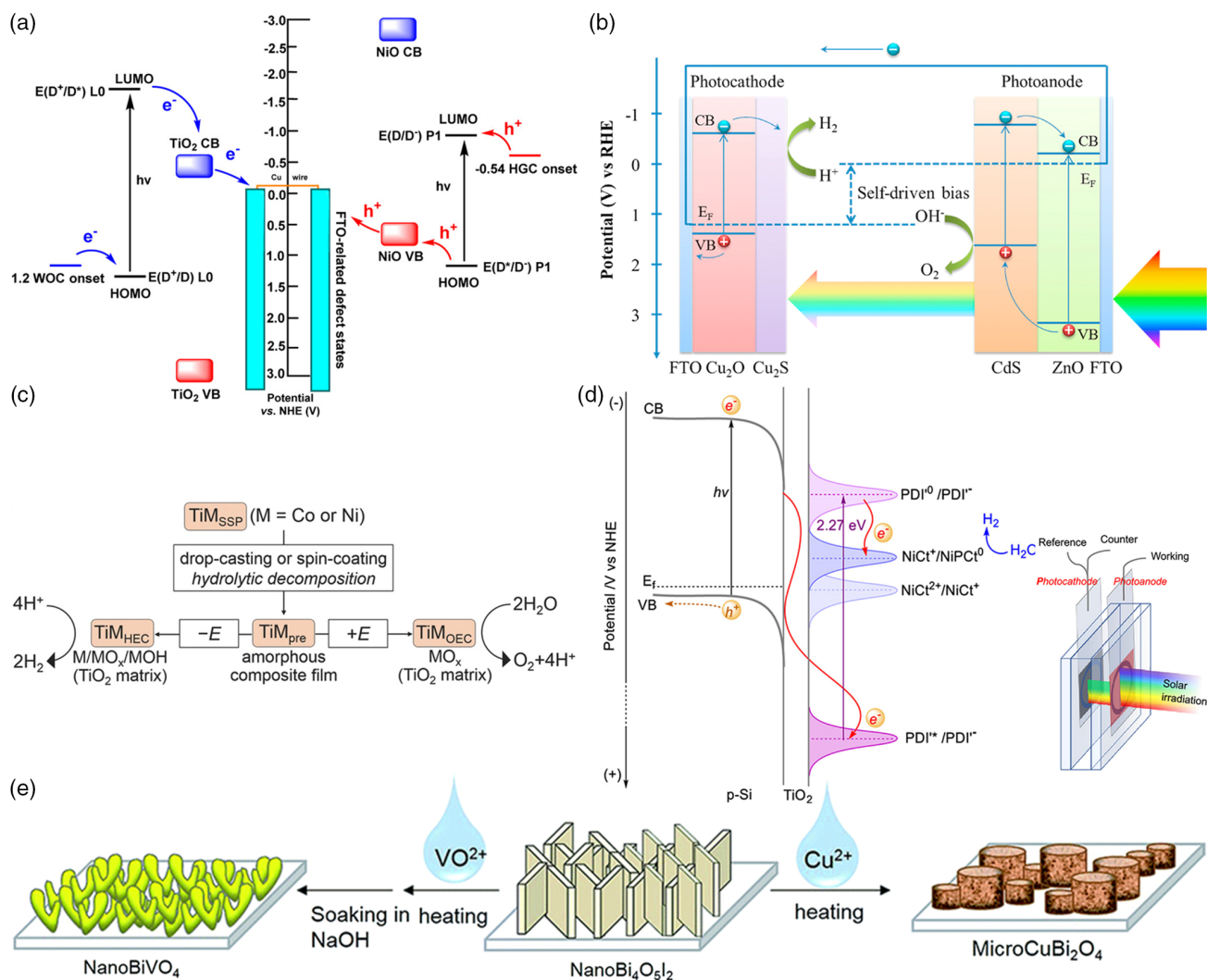

Figure 18. a) The energy diagram for the L0/Ru1/TiO_2–P1/Co1/NiO tandem cell at pH 7. L0 served as a dye sensitizer for TiO_2, and P1 acted as the photo-absorber for NiO. Reproduced with permission.[90] Copyright 2015, American Chemical Society. b) The energy band diagram of the self-driven tandem PEC cell consisting of a Cu_2O/Cu_2S photocathode and a ZnO/CdS photoanode. Reproduced with permission.[21] Copyright 2017, Elsevier. c) The synthesis mechanism of multi-functional TiNi and TiCo layers with a solution-processed single source precursor chemistry approach. Reproduced with permission.[92] Copyright 2015, WILEY-VCH. d) Energy band structure diagram for p–Si|Ti|TiO_2|-PDI-NiCt electrode, showing the energy alignment between p–Si CB, VB, and the redox states of the surface molecules (measured in pH 4.5 acetate (0.1 M) buffer with 0.9 M $NaClO_4$ as the supporting electrolyte). Reproduced with permission.[93] Copyright 2019, American Chemical Society. e) The conversion processes of nano$BiVO_4$ and micro$CuBi_2O_4$ from a single nano$Bi_4O_5I_2$ template. Reproduced with permission.[94] Copyright 2019, The Royal Society of Chemistry.

in the darkness. The sensitization of ZIF-67 and the addition of BP enhanced light absorption in the visible, even near-infrared region.

Cu_2O with a band gap of 2.0 eV is widely used as photocathode due to its earth-abundance, pleasant PEC performance, favorable band alignment, and non-toxicity.[95] Cu_2O as photocathode have been assembled with $BiVO_4$ photoanode for overall solar water splitting.[96] The same combination of photoelectrodes materials (Cu_2O and $BiVO_4$) was applied again but for the MXene type titanium carbide ($Ti_3C_2T_X$) modification at Cu_2O nanorods.[97] $Ti_3C_2T_X$ MXene was treated by a H_2/Ar gas to gain oxygen vacancies enriched H: $Ti_3C_2T_X$ MXene surface, which was demonstrated to exhibit better enhancement for Cu_2O photocathode than Au. The comparative test verified that the oxygen vacancies enhanced the conductivity and charge transfer sensibility. Based on the above optimization, the H:$Ti_3C_2T_X$/Cu_2O pair with $BiVO_4$ tandem PEC unassisted device yielded a STH efficiency of 0.55% and a considerable cathode photocurrent density of $-5.41 \, mA \, cm^{-2}$.[98,99]

A p–Cu_2O photocathode with a thin layer of Cu_2S and a n–ZnO/CdS nanowire photoanode were connected for self-driven solar water splitting (Figure 18b).[21] This tandem cell presented a photoconversion efficiency of 0.38% without applying a bias. The Cu_2S layer played a key role in the increase in cathodic photocurrent and the reduction in HER overpotential due to its enhancement in light absorption and charge transfer properties. A kind of coaxial nanowire Cu_2O/Ga_2O_3 buried p–n junction photocathode was reported with efficient light-harvesting in a broad spectral range and ≈80% external quantum yield.[100] For the design of this photocathode, a protection TiO_2 layer helped to stabilize the cathode and NiMo served as an HER catalyst. This optimized Cu/Cu_2O/Ga_2O_3/TiO_2/NiMo photocathode and a $BiVO_4$ based photoanode tandem PEC cell achieved a STH efficiency of ≈3% without applying external bias. The high PEC current density (≈10 $mA \, cm^{-2}$ at 0 V vs RHE) and photovoltage (onset over +1 V vs RHE) were ascribed to the good band alignment and the supressed interfacial recombination. This result provided a sound performance surpassing all known metal-oxide and silicon tandem systems. A kind of Z-scheme tandem PEC system consisting of a p–type carbon-modified Cu_2O nanoneedle photocathode and an n–type oxygen-deficient $TiO_{2−x}$ nanorod photoanode was fabricated for unassisted solar water splitting.[101] This tandem configuration exhibited 64.7 $\mu A \, cm^{-2}$ photocurrent density without any redox mediator and additional bias. The protective carbon layer, which was coated by a solution-based approach, improved the photostability of Cu_2O. In addition, the electrode conductivity was increased due to the oxygen vacancies in $TiO_{2−x}$ nanorods. It is worth mentioning that this work explored and compared two light incident modes. One was that the two photoelectrodes are simultaneously irradiated by the same incident light at the same time, and the other was that the incident light arrived on the photoanode surface and then reached the photocathode surface after the wavelength was filtered. It was proved that the latter showed better performance thanks to the rational filtration of light spectrum and provided some reference for the future optical path design. A p–type Cu_2O photocathode coupled with a three-dimensional ZnO/CdS/NiFe layered double hydroxide (LDH) photoanode tandem PEC cell was applied for overall solar water splitting.[102] Unlike the above works, this work was focused on the construction and optimization of photoanode. The introduction of CdS QDs (2.4 eV) boosted the light absorption in the visible region and enhanced charge separation due to the interface band bending. In the meanwhile, NiFe LDH served as a co-catalyst and provided plenty of active sites owing to its unique hierarchical mesoporous architecture. This coupled tandem configuration showed a photocurrent density of 0.4 $mA \, cm^{-2}$ and a STH efficiency of 0.5% without external bias. A kind of FeOOH modified TiO_2/$BiVO_4$ photoanode coupled with p–Cu_2O photocathode tandem PEC system was also prepared, and a photocurrent density of 0.12 $mA \, cm^{-2}$ without external bias was obtained.[103] In this case, TiO_2 inhibited the recombination of photo-generated electron and hole at the surface, and FeOOH served as both hole collector and OER catalyst.

P–type Si (p–Si, $E_{gap} = 1.1$ eV) is a promising candidate of photocathode material due to its optimal band gap, mature technology, high crystallinity, and low cost.[104] Diverse proof-of-concept tandem PEC devices have been prepared based on a Si-based photoelectrodes. A PEC tandem cell consisting of a haematite (α–Fe_2O_3) photoanode and Si photocathode with $NiFeO_x$ and TiO_2/Pt overlayers was prepared.[105] The characterized turn-on voltage of 0.45 (±0.01) V was obtained, and this movement in voltage verified that a facile regrowth strategy could help to improve the measured photovoltages on the photoanode. The origin of the low photovoltages was attributed to the short-range structural disorders near the surface of the photoanode. This α–Fe_2O_3/Si tandem device exhibited an overall efficiency of 0.91% without assisted bias, which represented the first example of unassisted solar water splitting using α–Fe_2O_3/Si as the sole light absorbers. A CoBi co-catalyzed undoped $BiVO_4$ photoanode (with double conformal TiO_2 layers) was coupled with a-Si photocathode and helped to achieve a STH efficiency of ≈3%.[106] In Reisner's study, P–Si|TiNi photocathode was coupled with nano WO_3|TiNi and nano $BiVO_4$|TiCo hybrid photoanodes, respectively.[92] Noting the limitations and challenges of the ALD method and sputtering technology for scalable electrodes preparation,[107] this work highlighted a highly versatile approach for preparing novel films over large scale, which could act as a protective layer, a kind of HER catalyst, and a kind of OER catalyst, respectively. More specifically, TiNi and TiCo layers prepared by a solution-processed single source precursor approach optimized the PEC performance of the whole device (as illustrated in Figure 18c). The p–Si|TiNi paired with $BiVO_4$|TiCo tandem system achieved a STH efficiency of 0.59% and a half-life photostability of 5 h. The p–Si nanowires have been utilized as the main material for photocathode and subsequently modified by a thin layer of Ti using physical vapor deposition and a protective layer of TiO_2 by ALD. In another work, the photocathode surface was modified with a perylene-diimide (PDI) derivative layer and a kind of Ni-based molecular HER catalyst.[93] Herein, PDI served as an electron transfer mediator thanks to its highly electron-deficient excited state, and a one-electron reduced shuttle was formed to effectively activate the catalyst. The output characteristics of p–Si were improved because its number and location of surface states were changed by the surface molecular modification.[108] The band structure and the involvement of the excited-state diagram are shown in Figure 18d. This heterojunction photocathode was then connected in series with a dye-sensitized core-shell structured

n–type SnO_2/TiO_2-based photoanode for PEC water splitting under a low applied bias. An initial photocurrent density of $\approx 0.3\,mA\,cm^{-2}$ was yielded without applied bias, and the photocurrent changed with the electrolyte pH value and ionic strength. It has been pointed out that the overall cell efficiency was limited by the performance of the photoanode. For the integrated tandem PEC cell, the photoanode was placed in the front of the cell so that the lower energy photons transmitted by the photoanode could be absorbed by the photocathode. Some other multi-element semiconductors were also developed for PEC water splitting. For example, Zhu et al. developed a Cu-doped $Zn_{0.3}Cd_{0.7}S$/graphene photocathode and assembled it with a WO_3/graphene photoanode for PEC water splitting.[109] They obtained a hydrogen spillover rate of $65.6\,\mu mol\,g^{-1}\,h^{-1}$ and an oxygen evolution rate of $12.3\,\mu mol\,g^{-1}\,h^{-1}$, respectively, where these values would correspond to 3.52 and $1.32\,mA\,g_{cat}^{-1}$, respectively. A $CuBi_2O_4$ photocathode and a $BiVO_4$ photoanode were put together for PEC water splitting, and the novelty is that both the electrodes were prepared from a single $Bi_4O_5I_2$ nanosheet template (Figure 18e).[94] A solvothermal deposition method was fully utilized in this work. $Bi_4O_5I_2$ could be converted to a textured $CuBi_2O_4$ by dropping the nanosheet template into a solution containing copper ions (Cu^{2+}), while coral-like $BiVO_4$ nanostructure could be obtained by drop-casting a vanadium ion-containing solution (VO^{2+}). The final electrode arrangement was obtained after an annealing process for these two electrodes. With modified cobalt-based catalysts in both photoelectrodes, the tandem system exhibited an overall photovoltage of $\approx 2.0\,V$ and showed a photocurrent density of $36\,\mu A\,cm^{-2}$ and a corresponding STH efficiency of 0.04% without an external bias. Guo et al. employed ternary sulfide $ZnIn_2S_4$ and $CuInS_2$ as photoelectrodes to fabricate bidirectional p–n heterojunction PEC tandem cells for unassisted water splitting. $ZnIn_2S_4/CuInS_2$ and $CuInS_2/ZnIn_2S_4$ were prepared by a simple two-step hydrothermal method, and they were used as photoanode and photocathode, respectively. This device achieved the photocurrent density of $0.06\,mA\,cm^{-2}$ with no bias. The new idea of bidirectional p–n heterojunction was thus proved to be available and of great value for the efficient preparation of electrodes. This conceptual result confirmed that a p–n heterojunction with different properties but the same semiconductor materials could be used in unassisted tandem PEC water splitting. Cu_2BaSnS_4 thin films synthesized by sol-gel spin-coating were investigated as photocathode materials and coupled with ZnO nanorods counter photoanode.[110] This tandem cell showed ≈ 4% photoconversion and photocurrent density of $-2.112\,mA\,cm^{-2}$ at 0 V vs RHE.

The encapsulation has been demonstrated as one of the efficient strategies for enabling the potential application of lead-halide perovskite as photoelectrodes in aqueous solutions. Reisner's group solved the limiting factors of scalability and durability of lead halide perovskite in PEC tandem system.[111] In this work, cesium formamidinium methylammonium (CsFAMA) triple cation mixed halide perovskite photovoltaic cells with NiO_x hole transport layer were employed to produce Field's metal-epoxy encapsulated photocathodes. Their stability (up to 7 h), photocurrent density ($-12.1 \pm 0.3\,mA\,cm^{-2}$ at 0 V vs RHE), and reproducibility enabled a matching combination with robust $BiVO_4$ photoanodes, resulting in a $0.25\,cm^2$ big PEC tandem cell with an excellent stability of up to 20 h and a bias-free STH efficiency of 0.35 ± 0.14%. As shown in

Figure 19, Edwardes Moore et al. interfaced [NiFeSe] hydrogenase from *Desulfovibrio vulgaris* Hildenborough, a highly active enzyme for H_2 generation, with a triple cation mixed halide perovskite, where it produced a photocurrent of $-5\,mA\,cm^{-2}$ at 0 V vs RHE during AM 1.5G irradiation with the stability for 12 h.[112] The positive onset potential of +0.8 V vs RHE allowed its combination with a $BiVO_4$ water oxidation photoanode to give a self-sustaining, bias-free PEC tandem system for overall water splitting (STH efficiency of 1.1%). This work provided a new benchmark for photocathodes and tandem PEC devices employing earth-abundant molecular H_2 production catalysts. The hybrid system demonstrated the potential for bias-free fuel production and established perovskites as a suitable photoelectrode material for the integration of biological catalysts.

This section combed from the concepts, selection of photoelectrodes materials, synthesis approaches of the electrodes, optimization strategies, and optical path design. Many efforts have been devoted to constructing proof-of-concept tandem devices to overcome the large external bias for overall water splitting, and it is undeniable that these designs are the foundation of future work. Most of the researchers still focused on optimizing the preparation procedures, photocatalytic performance, and stability of the entire device. While a large number of cases demonstrated the feasibility of the two-photoelectrode tandem system, only few tandem cells achieved a STH efficiency of above 10%, which is a fundamental requirement for commercialization.[113] Moreover, most of the overall water splitting tandem PEC systems do not evolve H_2 and O_2 gas products in a stoichiometric manner underline that some side reactions occur. Therefore, efforts are still needed to develop a high-efficient, satisfactory durable, and practical PEC tandem cell that ideally meets low-cost targets and enables universal preparation strategies.

The comparison of various properties, including synthesis method, band gaps of light absorbers and performance, for each system of the two-photoelectrode tandem cell is summarized in **Table 2**.

5. The Tandem Nanostructure of Plasmon Related Devices for PEC Water Splitting

The surface plasmon of noble metals presents critical applications in PEC water splitting. Excited by incident electromagnetic waves with the same frequency, the surface free electrons of metal nanostructures oscillate collectively. The sound local electromagnetic field, which is caused by the localized surface plasmon resonance (LSPR), can be used to improve the light absorption of adjacent semiconductors and regulate the spatial distribution of photo-generated electron-hole pairs in the semiconductor. The surface plasmon relaxation process from metal LSPR to semiconductor is generally divided into radiation loss and non-radiation loss. The energy transfer and charge transfer mechanisms involved have been extensively studied. Light scattering by radiation relaxation, thermal electron transfer, and resonance energy transfer by non-radiation relaxation are the three most common relaxation methods. Noble metal nanoparticles, especially Au and Ag, display an intense LSPR under excitation.[114] The resonant frequency of surface plasmon
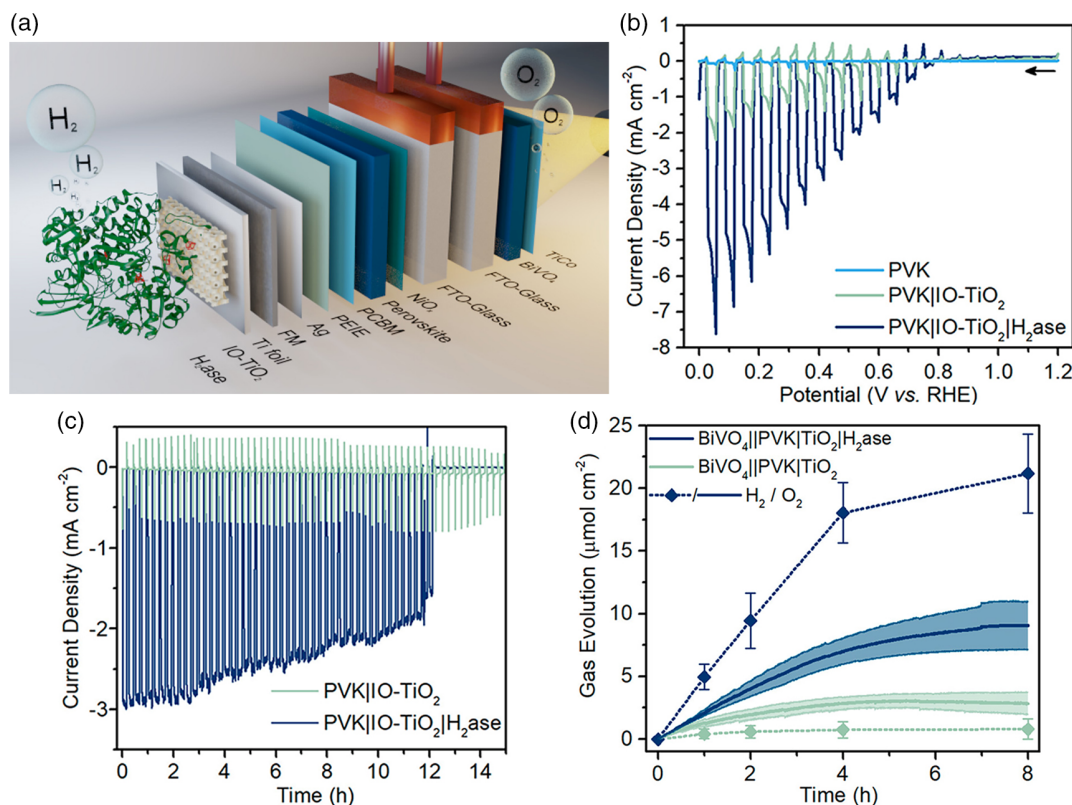
Figure 19. a) Schematic representation of the tandem PEC cell consisting of a FM-encapsulated perovskite photocathode with H_2-ase integrated into an IO–TiO$_2$ layer and a BiVO$_4$ photoanode. TiCo refers to the water oxidation layer precursor: [Ti$_4$O–(OEt)$_{15}$(CoCl)]. PCBM: [6,6]-phenyl-C$_{61}$-butyric acid methyl ester. PEIE: polyethylenimine. b) Representative LSV of PVK|IO-TiO$_2$ |H$_2$-ase (blue), PVK|IO-TiO$_2$(green), and PVK (light blue) electrodes with chopped illumination at a scan rate of 10 mV s^{-1}. Arrow indicates start of scan. c) Representative CPPE at E_{app} = +0.4 V vs RHE, with a dark period lasting 5 min following every 10 min of light exposure. d) Mean (N = 3) H$_2$ (dotted line with measurement points) and O$_2$ (solid line) evolution from CPPE repeats. Conditions: MES (50 mM, pH 6.0), KCl (50 mM), DvH [NiFeSe] H$_2$ ase (50 pmol), simulated solar light irradiation (AM 1.5G, 100 mW cm^{-2}), N$_2$ atmosphere, 25 °C. Reproduced with permission.[112] Copyright 2019, American Chemical Society.

nanostructures strongly depends on the morphology, geometric size, composition, as well as the surrounding dielectric environment.[115] Nevertheless, there will be electrolytic fluid corrosion and dissolution with ease for noble metals during the photocatalytic reaction.[116] Hence, tandem nanostructure of plasmon related devices including metal-semiconductor layered tandem structures and Janus structures are constructed for PEC water splitting, which also provided an ideal platform for investigating the special role of plasmon in the performance improvement for PEC water splitting.

Plasmonic PEC systems, in addition to the scattering effect in metallic nanostructures to increase the average optical path of photons in metal and semiconductor, thus improving the absorption efficiency of the system to incident light, exploit three roles of plasmonic metals, that are, the enhancement of electromagnetic field in the near-field, where LSPR effect can generate extremely strong electromagnetic field near metal nanoparticles (attenuation length is about 200 nm) to effectively improve the generation rate and separation efficiency of carriers in the semiconductor with close contact with them; the hot carriers injection between the interfaces,[3b,117] where the non-radiative decay of LSPR can generate a large number of thermal electrons to cross the Schottky barrier between metal and semiconductor and

migrate to the semiconductor, thus increasing the free electrons involved in catalytic reactions in the semiconductor and improving its catalytic performance; and the plasmon resonance energy transfer,[118] where the energy of a plasmonic oscillation is transferred from a plasmonic material to a semiconductor photocatalyst through an electromagnetic field or a dipole-dipole interaction to promote charge-carrier separation within a semiconductor photocatalyst, as shown in **Figure 20**. The metal LSPR plays a positive role in promoting the light absorption of adjacent semiconductors, enhancing the photoexcitation, promoting their charge separation, and injecting hot electrons.

5.1. The Plasmon-Based Layered Tandem Junction

The plasmon-based layered tandem junction is defined as a layered integrated device with plasmon metal and semiconductor, where plasmon metal films are composed of dense metal particles with sizes in the range of tens of nanometers, and strong LSPR could be excited. In consequence, however, the plasmon metal layer may not perform exactly the same in different positions. The Ag/Cu$_2$O/ZnO tandem triple-junction photoelectrode was constructed for enhanced hydrogen production (**Figure 21**a).[119] The insertion of an Ag film underneath the

Table 2. The synthesis method and performance for each system of the two-photoelectrode tandem cell.

The composition of nanostructure	Synthetic method	Band gaps of light absorbers	Performance	References
Double-sided tandem structure (TS) of CdS and CdSe cosensitized TiO$_2$ NDA photoelectrode	Hydrothermal method	2.4 eV for CdS; 2.3 eV for CdS; 3.2 eV for anatase, 3.0 eV for rutile	STH conversion efficiency of 2.78% at −0.63 V vs Ag/AgCl.	[84]
A monolithic (M) PEC device of Rh/TiO$_2$/AlInPO$_x$/AlInP/ GaInP-GaInAs/GaAs/RuO$_x$	Metal-organic vapor phase epitaxy, chemical etching, ALD and PEC deposition	3.2 eV for anatase, 3.0 eV for rutile; 2.53 eV for AlInP; 1.89 eV for GaInP; 0.74 eV for GaInAs; 1.515 eV for GaAs	The STH efficiency of 19.3% in an acidic electrolyte and a STH efficiency of 18.5% in a neutral electrolyte at 0 V, with an operating current of 15.7 mA cm^{-2}, which reached a value of 0.85 of the theoretical limit for PEC water splitting of this system.	[86]
n-Si/Metal-Oxide/WO$_3$/BiVO$_4$ MTS	Aerosol-assisted chemical vapor deposition (AA-CVD)	1.1 eV for Si; 2.7 eV for WO$_3$; 2.4 eV for BiVO$_4$	Unassisted Solar Water Splitting, a maximum photocurrent density of 0.3 mA cm^{-2} in 1.0 M KBr pH 9.3 buffer solution under AM 1.5G, with a STH of 0.37%. An average faradaic efficiency of ≈98%. The photocurrent density of >2.5 mA cm^{-2} at 1.23 V$_{RHE}$.	[87]
Organic dye-sensitized tandem PEC cell consisting of the photoanode of an organic dye L0 as photosensitizer and a molecular complex Ru1 as water oxidation catalyst on meso-porous TiO$_2$, and the photocathode of an organic dye P1 as photoabsorber and a molecular complex Co1 as hydrogen generation catalyst on nanostructured NiO.	Impregnation method	3.2 eV for anatase, 3.0 eV for rutile	Overall water splitting by visible light under neutral pH conditions without applying any bias. The photocurrent of 300 µA cm^{-2} under the conditions of the light intensity of 100 mW cm^{-2}, the applied bias potential of 0 V vs Ag/AgCl, and the electrolyte of 50 mM pH 7.0 phosphate buffer solution. An IPCE of 25% at 380 nm under neutral pH conditions.	[90]
A tandem cell (TC) for unassisted solar water splitting (USWS) consisting of the photocathode of H:Ti$_3$C$_2$T$_x$/Cu$_2$O CS ND and the photoanode of BiVO$_4$.	The reduction of H$_2$/Ar, a facile dip-coating method	2.55 eV for H:Ti$_3$C$_2$T$_x$; 2.1 eV for Cu$_2$O; 2.4 eV for BiVO$_4$	A photocurrent density of −5.41 mA cm^{-2} of H:Ti$_3$C$_2$T$_x$/Cu$_2$O at 0 V vs RHE under AM 1.5G. A STH of 0.55% for the tandem system.	[97]
A Cu$_2$O/Cu$_2$S-ZnO/CdS tandem PEC cell for USWS	Electrochemical deposition method, hydrothermal method, SILAR	2.1 eV for Cu$_2$O; 1.21 eV for Cu$_2$S; 3.2 eV for ZnO; 2.4 eV for CdS	An apparent photocurrent was observed for the tandem cell at zero bias, corresponding to a photoconversion efficiency of 0.38%.	[21]
A TC consisting of carbon-modified p–type Cu$_2$O nanoneedles and n–type TiO$_{2-x}$ nanorods for Z-scheme SWS	Anodization, annealing and hydrothermal growth.	2.1 eV for Cu$_2$O; 3.2 eV for anatase, 3.0 eV for rutile	A photocurrent density of 64.7 µA cm^{-2} in the absence of any redox mediator and external bias.	[101]
A TC for overall SWS containing a 3D ZnO/CdS/NiFe layered double hydroxide photoanode coupled with a Cu$_2$O photocathode	Hydrothermal method, SILAR, electrodeposition	3.2 eV for ZnO; 2.4 eV for CdS; 2.1 eV for Cu$_2$O	The photocurrent density of ZnO/CdS/NiFe LDH of 5.8 mA cm^{-2} at 0.9 V. For the tandem cell, a photocurrent density of 0.4 mA cm^{-2} with the STH conversion efficiency of 0.50%.	[102]

Table 2. Continued.

The composition of nanostructure	Synthetic method	Band gaps of light absorbers	Performance	References
A PEC TC composed of FeOOH/TiO$_2$/BiVO$_4$ and Cu$_2$O for USWS	Electrochemical deposition and PEC deposition	3.2 eV for anatase, 3.0 eV for rutile; 2.4 eV for BiVO$_4$; 2.1 eV for Cu$_2$O	An apparent photocurrent of 0.37 mA cm^{-2} at operating voltage of $+0.36$ V$_{RHE}$ without applied bias, corresponding to a photoconversion efficiency of 0.46%. The unassisted photocurrent density of 0.12 mA cm^{-2}, and the corresponding amounts of hydrogen and oxygen without bias of 2.36 μmol cm^{-2} and 1.09 μmol cm^{-2} after testing for 2.5 h. The IPCE of 92.5% of FeOOH/TiO$_2$/BiVO$_4$ at 450 nm, and of 42.0% of Cu$_2$O at 300 nm.	[103]
A PEC device with a haematite photoanode and Si photocathode to overall split water, with NiFeO$_x$ and TiO$_2$/Pt overlayers, respectively.	Hydrothermal method, calcination and drop casting	2.1 eV for Fe$_2$O$_3$; 1.1 eV for Si; 3.2 eV for anatase, 3.0 eV for rutile	An STH of 0.91%, the Faradaic efficiencies of H$_2$ and O$_2$ close to 100%, no obvious decay during the first 10 h.	[105]
A TC consisting of single source precursor (SSP) coating of a Si photocathode and a BiVO$_4$ photoanode for overall water splitting	Drop-casting or spin-coating	1.1 eV for Si; 2.4 eV for BiVO$_4$	An applied bias STH conversion efficiency of 0.59% and a half-life photostability of 5 h.	[92]
A water-splitting TC consisting of a perylene-diimide derivative (PDI) modified NW-structured p–type Si (p–Si) photocathode and a dye-sensitized SnO$_2$–TiO$_2$ photoanode	PVD, ALD	1.1 eV for Si; 3.2 eV for SnO$_2$; 3.2 eV for anatase, 3.0 eV for rutile	A photocurrent of the integrated photocathode of ≈ -1.0 mA cm^{-2} under zero applied bias vs NHE.	[93]
A TC consisting of a p–type Cu-doped Zn$_{0.3}$Cd$_{0.7}$S/graphene photocathode and an n–type WO$_3$/graphene photoanode	spreading a portion of viscous suspension and calcination	2.7 eV for WO$_3$	The rates of hydrogen and oxygen evolution of 65.6 and 12.3 μmol g^{-1} h^{-1} (80.5 and 15.1 μmol cm^{-2} h^{-1}), respectively.	[109]
A TC consisting of CuBi$_2$O$_4$ and BiVO$_4$ synthesized from a single Bi$_4$O$_5$I$_2$ nanosheet template	Drop-casting with a follow-up heat treatment	1.5–1.8 eV for CuBi$_2$O$_4$; 2.4 eV for BiVO$_4$; 2.0 eV for Bi$_4$O$_5$I$_2$	A bias-free photocurrent of 36 μA cm^{-2}, corresponding to a STH efficiency of 0.04%.	[94]
A TC of Cu$_2$BaSnS$_4$ photoanode coupled with ZnO ND photocathode	Sol-gel spin-coating	1.9 eV for Cu$_2$BaSnS$_4$; 3.2 eV for ZnO	-2.112 mA cm^{-2} at 0 V vs RHE with the photoconversion efficiency of ≈ 4%.	[110]

Cu$_2$O film increased the photocurrent of the electrode to 1100 μA cm^{-2}. The strong localized electromagnetic field and the alignment of the band level were found responsible for this enhancement (Figure 21a). The hot electrons excited by LSPR from Ag transferred to Cu$_2$O's CB and were further captured for water reduction. CdS–Au–TiO$_2$ sandwich nanorod arrays photoanode presented an enhanced hydrogen generation compared with TiO$_2$ nanorod arrays, which obtained a photocurrent density of 4.07 mA cm^{-2} at 0 V vs Ag/AgCl under full solar spectrum irradiation and a maximum solar-to-chemical energy conversion efficiency of 2.8%.[120] The middle layer Au nanoparticles between the TiO$_2$ nanorod and the CdS QDs played a dual role of an electron relay and a plasmonic photosensitizer, both of which could help to enhance the solar-to-chemical energy conversion efficiency. As shown in Figure 21b, when excited by light with a wavelength below 525 nm, the photo-generated electrons flew from CdS QDs to Au nanoparticles and then transferred to TiO$_2$ nanorods. Whereas, when the irradiation light wavelength increased from 525 to 725 nm, the LSPR of Au was excited and enabled hot electrons to transfer to TiO$_2$. This layered tandem junction was a model of sound design, which fully proved the wavelength dependence of the charge transport mechanism of the plasmon-based tandem structure. In another example, a photoelectrode was fabricated by depositing Au nanoparticles arrays and PZT films on ITO substrates.[3b] Herein, PZT was employed because PZT is a kind of ferroelectric material and its electrical properties could be tuned with polarization (see above Chapter 3.2.3). By manipulating different positions of
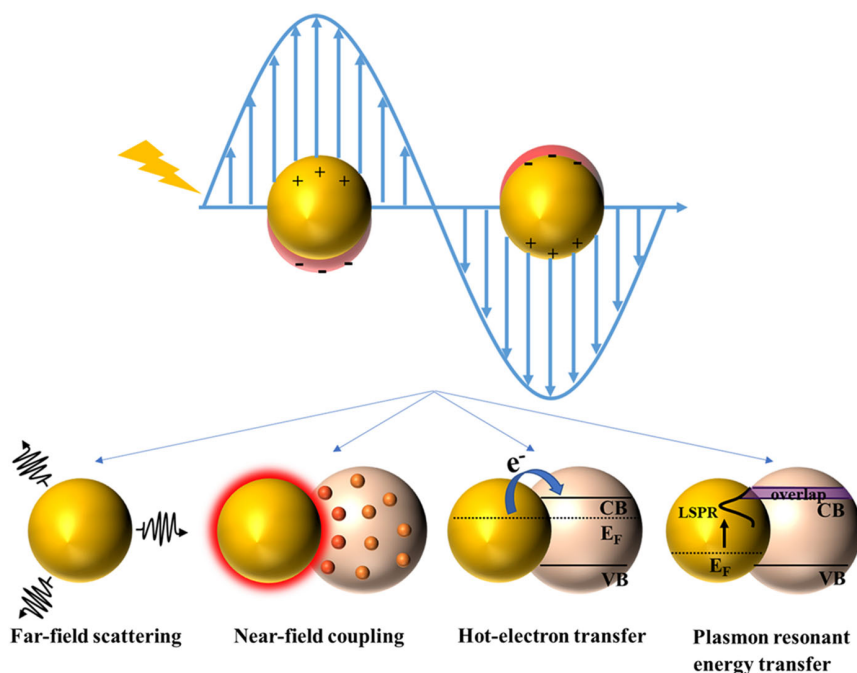
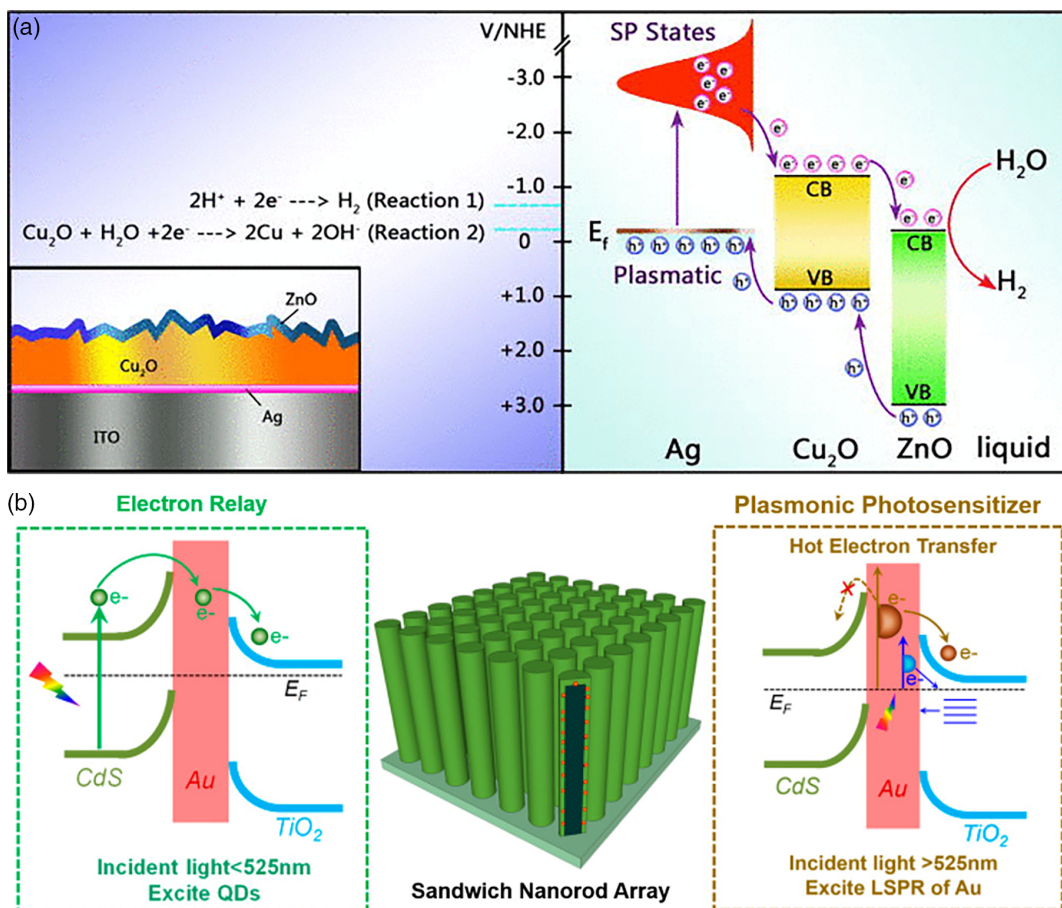**Figure 20.** Enhancement mechanisms for plasmon-based devices.

Figure 21. a) The energy band levels and the charge transfer process in the Ag/Cu$_2$O/ZnO tandem triple-junction photoelectrode on the NHE scale. Reproduced with permission.[119] Copyright 2015, AIP Publishing. b) Illustration for the CdS–Au–TiO$_2$ sandwich nanorod array and the dual role of Au nanoparticles layer with different incident light wavelength. Reproduced with permission.[120] Copyright 2014, American Chemical Society.

the nano-Au array, three kinds of hybrids (i.e., ITO/nano-Au/PZT, ITO/PZT/nano-Au/PZT, and ITO/PZT/nano-Au) were fabricated and it was found that ITO/nano-Au/PZT presented the best performance. The ITO/PZT/nano-Au/PZT electrodes were applied to demonstrate that the short-circuit photocurrent could be tuned by nearly an order of magnitude from 2.4 to $16.7 \, \mu A \, cm^{-2}$ when the pre-poling bias was switched from $+10$ to $-10 \, V$. Schemes to visualize the mechanism for the injected hot-electron transfer from PZT films to the electrolyte for the two poling configurations are shown in **Figure 22**a. The presence of Au nanoparticle arrays facilitated the charge transfer between Au and PZT, which was directly verified by the ultrafast dynamic charge transfer. For example, a CdS/Au pillar/truncated-pyramid (PTP) array photoanode was prepared,[121] where Au pillars were set on a truncated-pyramid in each unit, and a uniform CdS film was subsequently deposited to form a macroscopic core-shell tandem structure. Superior optical absorption of about 95% within a wide wavelength range was demonstrated. The continuous incident photon to current efficiency (IPCE) enhancement from 300 to 600 nm occurred in CdS/Au PTPs, and the photocurrent density of it reached up to $3.5 \, mA \, cm^{-2}$ at $-0.4 \, V$ vs Ag/AgCl. It has been concluded that there were two different modes for improvement under the

incident light above and below 450 nm: SPR enhancement modes worked in the range above 450 nm while the photonic enhancement modes dominated below 450 nm. In this tandem structure, the aspect ratio of PTP in Au PTP and CdS thickness have affected light absorption. This designed plasmonic core/shell PTP structure could be easily extended to other PEC cells. The cross-sectional SEM image of the CdS/Au PTPs array and the enhanced electric field is shown in Figure 22b.

It has been identified that AuAg alloy nanostructures could extend the utilization of visible light and enhance the catalytic properties of noble metals. Hence, an AuAg alloy was sandwiched between the homojunction of n-Cu_2O and p-Cu_2O for improved water reduction.[122] The protection of the two-terminal semiconductor protected the plasmonic AuAg alloy from photocorrosion during PEC reaction. The AuAg alloy played a role both as an electron relay and an electron-hole generation promoter for Cu_2O, and the interfacial charge transfer mechanism was revealed with synchrotron-based in situ X-Ray absorption spectroscopy (XAS). In this tandem structured photocathode, an extremely positive onset potential of 0.8 V vs RHE and a photocurrent density of $-2.0 \, mA \, cm^{-2}$ was obtained, which is comparable with measurements from water reduction catalysts. This plasmonic photosensitization effect within a p-n homojunction
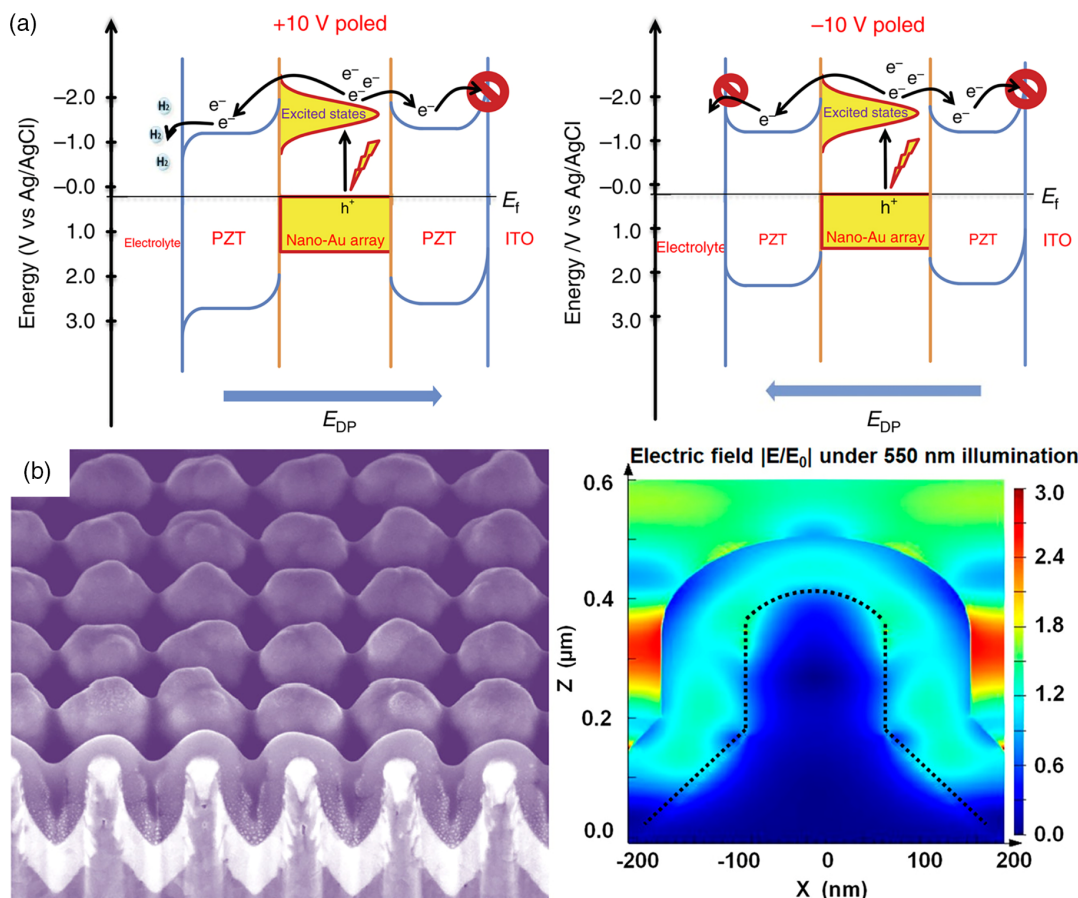

Figure 22. a) Schematic band structure and the injected hot-electron transfer path at different pre-polarization biases. Reproduced with permission.[3b] Copyright 2016, Springer Nature. b) The cross-sectional SEM image and the simulated enhanced electric field distribution using the FDTD method of the CdS/Au PTP arrays. Reproduced with permission.[121] Copyright 2017, American Chemical Society.

provides a new direction for improving the efficiency of PEC water splitting devices.

5.2. The Janus Hetero-Nanostructures (HNs) of Plasmon-Based Devices

The asymmetric Janus nanostructure can integrate two materials with entirely different physicochemical properties on one nanoparticle and could facilitate synergistic coupling of diverse functions inherited by their comprised nanocomponents.[123] In our definition, the plasmon-based Janus HNs mainly refer to the plasmon metal nanostructures whose two sides are in two different dielectric environments, thus generating novel optical properties and catalytic performance. These Janus HNs possess not only increased charge injection and optical path length but also enhanced light absorption from visible to NIR range.[124] The synthesis of plasmon-based Janus HNs needs to be adequately designed. Jiang et al. achieved controllable self-assembly of nanoparticles in aqueous solutions by balancing the hydrophobic and hydrophilic moieties.[125] They synthesized Janus Au-Fe_3O_4 dumbbell nanocrystals (<20 nm) with the hydrophobic ligands and negatively charged hydrophilic ligands coated on Au and

Fe_3O_4 lobe, respectively. By tuning size ratio, surface coating, external conditions, and additional growth of Au nanocrystal (**Figure 23**a), these superstructures exhibited a different level of enhancement in Au SPR. In addition, a red-shift in SPR was triggered due to the solid interparticle plasmonic coupling. This self-assembly progress of biphasic Janus dumbbell nanocrystals offers a significant reference for plasmon-based Janus HNs. Arrays of TiO_2-Au Janus HNs were designed and fabricated with the assistance of binary-pore anodic aluminium oxide templates.[18] A sequential process of over-etching and electrodeposition was employed to control the structural parameters of TiO_2-Au Janus HNs. The increased photocurrent density of 1.7 mA cm^{-2} at 1.23 V vs RHE and enhanced H_2 evolution performance of 17.5 $\pm$ 2.6 µmol h^{-1} cm^{-2} were mainly determined by LSPR induced hot electron injection and strong plasmon resonance energy transfer (PRET) effect at the junction area between TiO_2 nanotubes and Au nanorods, which was demonstrated by theoretical finite-difference time-domain (FDTD) modeling (Figure 23b). Meanwhile, the exposed part of plasmon metal and semiconductor could also facilitate charge carrier transfer from HNs to their adjacent HER or OER promoters in electrolytes. The visible light extinction difference between Au-SnS_2 Janus and core-shell structures was also demonstrated,
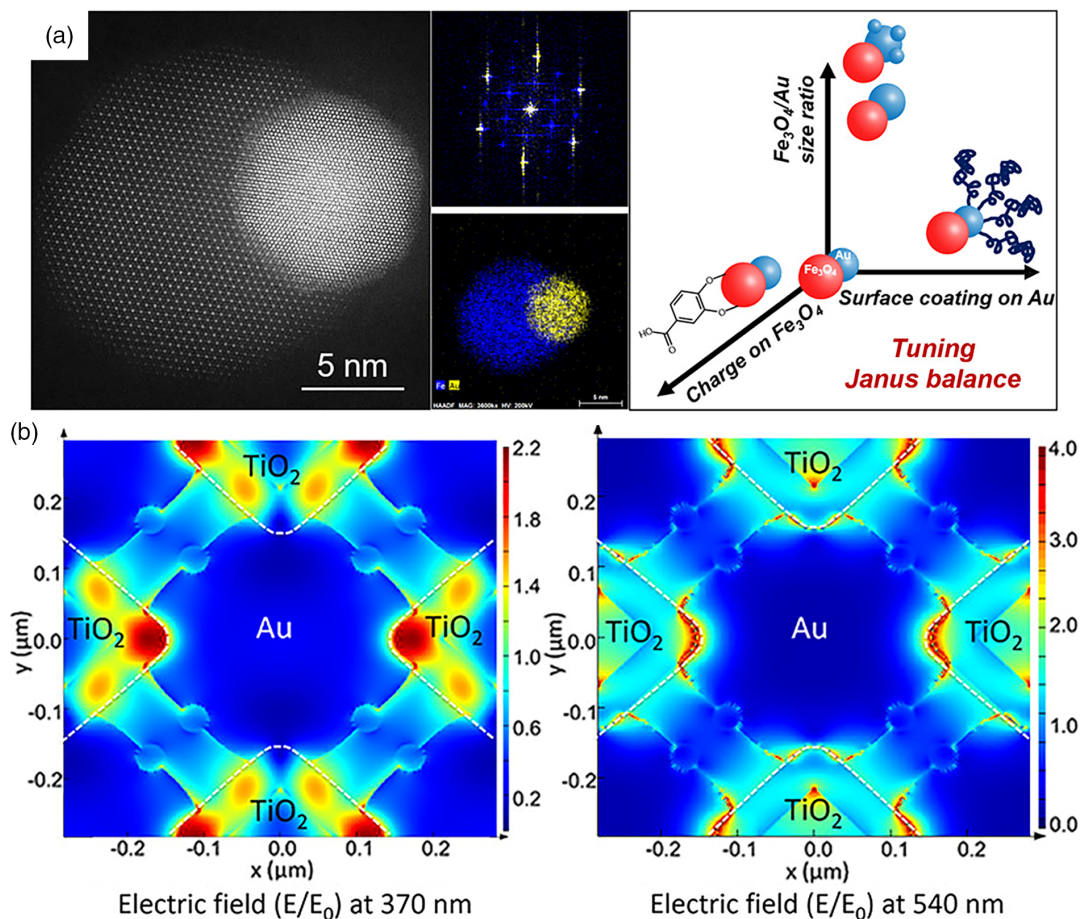

Figure 23. a) HAADF-STEM pattern of Au-Fe_3O_4 and the system regulation means. Reproduced with permission.[125] Copyright 2019, American Chemical Society. b) The cross-sectional view of FDTD simulated electric field (|E/E_0|) distributions for the TiO_2–Au Janus HNs at 370 and 540 nm. Reproduced with permission.[18] Copyright 2018, American Chemical Society.

and the former was found out to exhibit better performance.[126] This difference in performance was attributed to the difference in LSPR enhancement and the lifetime of photo-generated carriers. The absorption spectrum and photoluminescence (PL) spectrum revealed the more significant LSPR intensities and the shorter lifetime in Janus nanostructures. Correspondingly, the Janus nanostructures showed more effective catalytic performance in visible light irradiation.

Plasmon-based tandem PEC devices have exhibited preferable PEC water splitting performance by taking advantage of several specific mechanisms. Good contact between noble plasmon metals and semiconductors still requires further design. Picking a new candidate plasmon material (such as graphene) and designing other nanostructures conducive to the full play of LSPR features may be the next research focus.

The comparison of various pr7operties, including synthesis method, band gaps of light absorbers and performance, for each system of the tandem nanostructure of plasmon related devices is listed as **Table 3**.

6. Summary and Perspectives

To sum up, this review highlights several typical materials, processes and architectures of tandem PEC configurations supposed to boost PEC water splitting, including core/shell tandem nanostructured cells, two-photoelectrode tandem systems, and plasmon-based tandem devices. The material layer assembly distinguishes these different forms of tandem systems. Their essence is multi-absorber or tandem device structures of light

Table 3. The synthesis method and performance for each system of the tandem nanostructure of plasmon related devices.

The composition of nanostructure	Synthetic method	Band gaps of light absorbers	Performance	References
Ag/Cu$_2$O/ZnO tandem triplejunction PEC cell	Electrochemical deposition and ALD	2.1 eV for Cu$_2$O; 3.2 eV for ZnO	The photocurrent of 1100 μA cm^{-2}.	[119]
CdS–Au–TiO$_2$ sandwich NDA photoanode	Hydrothermal method and chemical bath deposition	2.4 eV for CdS; 3.2 eV for anatase, 3.0 eV for rutile	IPCE of 85% at 375 nm at 0 V vs Ag/AgCl (0.25 M Na$_2$S and 0.35 M Na$_2$SO$_3$, pH 12).	[120]
			A photocurrent density of 4.07 mA cm^{-2} at 0 V vs Ag/AgCl.	
			A maximum solar-to-chemical energy conversion efficiency (η) of ≈2.8% at 0.56 V vs Ag/AgCl	
ITO/nano-Au arrays/Pb(Zr,Ti)O$_3$ (PZT)	Prepatterned anodization process, electron beam evaporation, and a sol-gel method.	3.5 eV for Pb(Zr,Ti)O$_3$	The photocurrent density of ≈10 μA cm^{-2} at 0.6 V vs Ag/AgCl (0.1 M Na$_2$SO$_4$)	[3b]
			The photocurrent density could be tuned from 2.4 to 16.7 μA cm^{-2} at the intensity of 100 mW cm^{-2} by switching the poling conditions from −10 to +10 V.	
CdS/Au PTP array photoanode	Imprinted template, physical vapor deposition and electrodeposition	2.4 eV for CdS	The photocurrent density of 3.5 mA cm^{-2} at −0.4 V vs Ag/AgCl (0.2 M Na$_2$S and 1.0 M Na$_2$S$_2$O$_3$, AM 1.5G).	[121]
Sandwich-nanostructured n–Cu$_2$O/AuAg/p–Cu$_2$O photocathode	Electrodeposition and magnetron sputtering	2.1 eV for Cu$_2$O	An extremely positive onset potential of 0.8 V vs RHE and a photocurrent density of −2.0 mA cm^{-2}	[122]
Arrays of TiO$_2$/Pt NPs-Au Janus heteronanostructures photoanode	Imprinted templates, ALD and electrodeposition	3.2 eV for anatase, 3.0 eV for rutile	The photocurrent density of 1.7 mA cm^{-2} at 1.23 V vs RHE (0.5 M Na$_2$SO$_4$, pH = 6.8, AM 1.5G).	[18]
			IPCE with a peak of 1.21% at around 540 nm.	
			The hydrogen evolution rate of 17.5 ± 2.6 μmol h^{-1} cm^{-2}.	
			≈96% degradation of the MB dye after 50 min of visible light.	
Plasmonic Ag@Ag$_3$(PO4)$_{1-x}$ CS nanoparticle photosensitized ZnO NDA photoanodes	Electrodeposition method and in situ electrochemical deposition	2.43 eV for Ag$_3$(PO$_4$)$_{1-x}$	The IPCE is up to 60% at 400 nm of 0.4 V vs Pt.	[116]
			The photocurrent of 3.1 mA cm^{-2} at 0.6 V vs RHE (0.5 M Na$_2$SO$_4$, pH of 6.8, AM 1.5G).	
			O$_2$ evolution of 34 mmol h^{-1}.	
			Good stability (a minimal degradation rate of only 1.3% after 10 h of continuous running) in the water-oxidation process at 0.6 V.	

absorbers and accelerators (such as charge transfer medium, co-catalysts, and so on). The tandem PEC systems undoubtedly overcome some shortcomings of single absorber PEC cells involving limited absorption range of the spectrum, low potential efficiency, and starveling material choices due to the high band gaps, which are needed for reaction kinetics. For direct water splitting in tandem configurations, optimized bandgap combinations of ≈ 1.1 and 1.7 eV can provide sufficient photovoltage whilst efficiently utilizing the solar spectrum. Non-radiative, in particular, interfacial recombination need to be suppressed, such that the only losses in performance are carrier thermalization and radiative recombination. To date, quite a few proof-of-concept tandem PEC configurations have been proposed and some of which have achieved considerable water splitting performance, but unfortunately, the vast majority are still limited by the STH efficiency of less than 10%. Fulfilling commercially available requirements is the ultimate goal of all PEC water splitting devices. There is still a long way off. Therefore, combined with the research progress of the developed tandem structures, several constructive suggestions and prospects are given as follows: 1) Most fundamentally, screening new candidate materials is crucial for preferable PEC performance. As outlined in the text, Si, metal oxides, chalcogenides, and III–V compounds are the most widely used photoelectrode materials. Engineering elemental doping or defects is an important and promising approach to change the band structure of semiconductors or modulate their electronic structures to a suitable state favorable for PEC water splitting. Theoretical calculations of material energy band structure, electronic structures, and hydrogen evolution reaction kinetics have become a meaningful way to pre-screen candidate photoelectrode materials. The innermost selection mechanism still needs to be explained with the assistance of calculation based on density functional theory and experimental verification in parallel. Moreover, the preparation strategy of photoelectrode materials needs to be upgraded to an easy-to-scale and straightforward method: 2) For core-shell tandem nanostructured photoelectrodes, making full use of the advantages of core and shell materials is critical to enhance the activity and stability of such photoelectrodes. Usually, the optimal core/shell photoelectrodes are developed through lots of experimental tests based on band theory and material properties. Considering the complexity in experiment and analysis, the highly efficient prediction and synthetic techniques are important for rapidly screening and fabricating best-matched core/shell configurations. Moreover, as the growth and configuration of the overlayer are closely related to the surface composition and structure of the underlying core materials, which can directly affect the performance of the core/shell photoelectrode, the material synergy strategies that can coordinate the interaction between core and the overlayer are needed: 3) In a tandem PEC cell consisting of the two photoelectrodes, it now appears that the ability to achieve overall water splitting without the assisted bias has been commonly obtained in most as-envisioned devices. However, the slow water oxidation kinetics are still unfavorable for stoichiometric hydrogen and oxygen evolution. Further increasing the overlapping area of the onset potential of photoanode and photocathode still needs substantial efforts to settle open questions on the way of manufacturing two-photoelectrodes PEC tandem devices. Constructing an optimized system that balances band alignment, cost, and

stability is the mainstream direction of current and even future two-photoelectrode tandem devices; 4) For plasmon-based tandem PEC devices, several plasmon decay mechanisms and their corresponding contributions to the improved PEC performance are beyond classical limits, and the plasmonic nanoarrays offer unique advantages. Only some one-dimensional plasmonic nanostructures are able to provide potential possibilities for extending the response spectrum of the PEC system to visible light and even NIR region. Building more exclusive metal-semiconductor contact structures using tip-enhanced LSPR may be the direction of future efforts. Besides noble metals in the traditional sense, plasmonic metal alloy nanostructures and metal nitrides provide promising alternatives. Furthermore, 2D plasmonic materials (e.g., graphene) may be able to contribute to reduce cost, enhance bonding, and reduce interfacial barriers; and 5) In addition to the development of PEC water splitting systems with high efficiency and stability, systematic investigation of the interfacial excitation/carrier transport-injection mechanisms of photoelectrodes should be another critical issue to be addressed, especially for photoelectrodes of tandem nanostructured systems with compound materials. Although various characterization methods have been employed, such as time-resolved spectroscopy, X-Ray photoelectron spectroscopy, in situ TEM, the comprehensively experimental and theoretical studies should be designed and conducted in the future. Maybe in-situ characterization strategies that can perform under light irradiation and bias potential would be an effective direction.

Conflict of Interest

The authors declare no conflict of interest.

[1] F. E. Osterloh, *Chem. Soc. Rev.* **2013**, *42*, 2294.

[2] A. Fujishima, K. Honda, *Nature* **1972**, *238*, 37.

[3] a) D. Cao, N. Nasori, Z. Wang, Y. Mi, L. Wen, Y. Yang, S. Qu, Z. Wang, Y. Lei, *J. Mater. Chem. A* **2016**, *4*, 8995; b) Z. Wang, D. Cao, L. Wen,

R. Xu, M. Obergfell, Y. Mi, Z. Zhan, N. Nasori, J. Demsar, Y. Lei, *Nat. Commun.* **2016**, *7*, 10348; c) B.-T. Zhang, J. Liu, S. Yue, Y. Teng, Z. Wang, X. Li, S. Qu, Z. Wang, *Appl. Catal., B* **2017**, *219*, 432; d) Z. Liu, A. Tang, J. Liu, D. Zhu, X. Shi, Q. Kong, Z. Wang, S. Qu, F. Teng, Z. Wang, *J. Mater. Chem. A* **2018**, *6*, 18649; e) Z. Liu, J. Liu, Y. Huang, J. Li, Y. Yuan, H. Ye, D. Zhu, Z. Wang, A. Tang, *Nanoscale* **2019**, *11*, 158.

[4] a) F. Xie, J. Gao, N. Wang, *J. Semicond.* **2017**, *38*, 073002; b) C. Ding, Y. Zhang, F. Liu, Y. Kitabatake, S. Hayase, T. Toyoda, K. Yoshino, T. Minemoto, K. Katayama, Q. Shen, *Nano Energy* **2018**, *53*, 17; c) Y. Zhao, T. L. Chen, L. Xiao, M. A. Kolaczkowski, L. Zhang, L. M. Klivansky, V. Altoe, B. Tian, J. Guo, X. Peng, Y. Tian, Y. Liu, *Nano Energy* **2018**, *53*, 345; d) J. Wang, J. Zhang, Y. Xiao, T. Xiao, R. Zhu, C. Yan, Y. Fu, G. Lu, X. Lu, S. R. Marder, X. Zhan, *J. Am. Chem. Soc.* **2018**, *140*, 9140; e) Y. Mi, L. Wen, Z. Wang, D. Cao, Y. Fang, Y. Lei, *Appl. Catal., B* **2015**, *176*, 331.

[5] S. Choudhary, S. Upadhyay, P. Kumar, N. Singh, V. R. Satsangi, R. Shrivastav, S. Dass, *Int. J. Hydrogen Energy* **2012**, *37*, 18713.

[6] P.-Y. Hsieh, J.-Y. Wu, T.-F. M. Chang, C.-Y. Chen, M. Sone, Y.-J. Hsu, *Arabian J. Chem.* **2020**, *13*, 8372.

[7] Y. Chen, X. Feng, Y. Liu, X. Guan, C. Burda, L. Guo, *ACS Energy Lett.* **2020**, *5*, 844.

[8] S. Wang, P. Chen, Y. Bai, J. H. Yun, G. Liu, L. Wang, *Adv. Mater.* **2018**, *30*, 1800486.

[9] a) M. Zhong, T. Hisatomi, Y. Kuang, J. Zhao, M. Liu, A. Iwase, Q. Jia, H. Nishiyama, T. Minegishi, M. Nakabayashi, *J. Am. Chem. Soc.* **2015**, *137*, 5053; b) R. Liu, Z. Zheng, J. Spurgeon, X. Yang, *Energy Environ. Sci.* **2014**, *7*, 2504.

[10] a) X. Yang, A. Wolcott, G. Wang, A. Sobo, R. C. Fitzmorris, F. Qian, J. Z. Zhang, Y. Li, *Nano Lett.* **2009**, *9*, 2331; b) G. Wang, H. Wang, Y. Ling, Y. Tang, X. Yang, R. C. Fitzmorris, C. Wang, J. Z. Zhang, Y. Li, *Nano Lett.* **2011**, *11*, 3026.

[11] a) P. Zhang, L. Gao, X. Song, J. Sun, *Adv. Mater.* **2015**, *27*, 562; b) T. Hannappel, M. M. May, H.-J. Lewerenz, in *Photoelectrochemical Water Splitting: Materials, Processes and Architectures* (Eds: H.-J. Lewerenz, L. Peter), The Royal Society of Chemistry, London **2013**, Chapter 9, pp. 223–265; c) J. Kupec, R. L. Stoop, B. Witzigmann, *Opt. Express* **2010**, *18*, 27589.

[12] a) M. Pavlenko, K. Siuzdak, E. Coy, M. Jancelewicz, S. Jurga, I. Iatsunskyi, *Int. J. Hydrogen Energy* **2017**, *42*, 30076; b) Y. J. Hwang, C. H. Wu, C. Hahn, H. E. Jeong, P. Yang, *Nano Lett.* **2012**, *12*, 1678.

[13] a) F. Cui, Y. Zhang, H. A. Fonseka, P. Promdet, A. I. Channa, M. Wang, X. Xia, S. Sathasivam, H. Liu, I. P. Parkin, H. Yang, T. Li, K.-L. Choy, J. Wu, C. Blackman, A. M. Sanchez, H. Liu, *ACS Appl. Mater. Interfaces* **2021**, *13*, 30950; b) L. Gao, Y. Cui, J. Wang, A. Cavalli, A. Standing, T. T. T. Vu, M. A. Verheijen, J. E. M. Haverkort, E. P. A. M. Bakkers, P. H. L. Notten, *Nano Lett.* **2014**, *14*, 3715.

[14] P. P. Kunturu, C. Zachariadis, L. Witczak, M. D. Nguyen, G. Rijnders, J. Huskens, *ACS Appl. Mater. Interfaces* **2019**, *11*, 41402.

[15] a) S. Deng, Y. Zhong, Y. Zeng, Y. Wang, Z. Yao, F. Yang, S. Lin, X. Wang, X. Lu, X. Xia, J. Tu, *Adv. Mater.* **2017**, *29*, 1700748; b) D. Chen, Z. Liu, S. Zhang, *Appl. Catal., B* **2020**, *265*, 118580; c) M. Li, T. Liu, Y. Yang, W. Qiu, C. Liang, Y. Tong, Y. Li, *ACS Energy Lett.* **2019**, *4*, 1983; d) Y.-J. Dong, J.-F. Liao, Z.-C. Kong, Y.-F. Xu, Z.-J. Chen, H.-Y. Chen, D.-B. Kuang, D. Fenske, C.-Y. Su, *Appl. Catal., B* **2018**, *237*, 9.

[16] a) K. Xu, A. Chatzitakis, E. Vøllestad, Q. Ruan, J. Tang, T. J. Norby, *Int. J. Hydrogen Energy* **2019**, *44*, 587; b) B. Shan, M. K. Brennaman, L. Troian-Gautier, Y. Liu, A. Nayak, C. M. Klug, T.-T. Li, R. M. Bullock, T. J. Meyer, *J. Am. Chem. Soc.* **2019**, *141*, 10390; c) M. S. Prévot, K. Sivula, *J. Phys. Chem. C* **2013**, *117*, 17879.

[17] D. V. Dao, T. T. D. Nguyen, P. Uthirakumar, Y.-H. Cho, G.-C. Kim, J.-K. Yang, D.-T. Tran, T. D. Le, H. Choi, H. Y. Kim, Y.-T. Yu, I.-H. Lee, *Appl. Catal., B* **2021**, *286*, 119947.

[18] L. Wen, R. Xu, C. Cui, W. Tang, Y. Mi, X. Lu, Z. Zeng, S. L. Suib, P. X. Gao, Y. Lei, *Nano Lett.* **2018**, *18*, 4914.

[19] H. Dotan, O. Kfir, E. Sharlin, O. Blank, M. Gross, I. Dumchin, G. Ankonina, A. Rothschild, *Nat. Mater.* **2013**, *12*, 158.

[20] M. Z. Ansari, S. Singh, N. Khare, *Solar Energy* **2019**, *181*, 37.

[21] Z. Bai, Y. Zhang, *J. Alloys Compd.* **2017**, *698*, 133.

[22] I. Narkeviciute, P. Chakthranont, A. J. M. Mackus, C. Hahn, B. A. Pinaud, S. F. Bent, T. F. Jaramillo, *Nano Lett.* **2016**, *16*, 7565.

[23] J. Cao, J. Xing, Y. Zhang, H. Tong, Y. Bi, T. Kako, M. Takeguchi, J. Ye, *Langmuir* **2013**, *29*, 3116.

[24] Y. Wang, H. Shi, K. Cui, L. Zhang, S. Ge, J. Yu, *Appl. Catal., B* **2020**, *275*, 119094.

[25] D. Shao, Y. Cheng, J. He, D. Feng, L. Zheng, L. Zheng, X. Zhang, J. Xu, W. Wang, W. Wang, *ACS Catal.* **2017**, *7*, 5308.

[26] U. V. Ghorpade, M. P. Suryawanshi, S. W. Shin, J. Kim, S. H. Kang, J.-S. Ha, S. S. Kolekar, J. H. Kim, *J. Mater. Chem. A* **2018**, *6*, 22566.

[27] R. Pan, J. Liu, Y. Li, X. Li, E. Zhang, Q. Di, M. Su, J. Zhang, *J. Mater. Chem. A* **2019**, *7*, 23038.

[28] a) A. T. Sivagurunathan, S. Adhikari, D.-H. Kim, *Nano Energy* **2021**, *83*, 105802; b) J.-B. Pan, S. Shen, L. Chen, C.-T. Au, S.-F. Yin, *Adv. Funct. Mater.* **2021**, *31*, 2104269.

[29] a) C. Jiang, S. J. A. Moniz, A. Wang, T. Zhang, J. Tang, *Chem. Soc. Rev.* **2017**, *46*, 4645; b) O. Supplie, M. M. May, H. Stange, C. Höhn, H.-J. Lewerenz, T. Hannappel, *J. Appl. Phys.* **2014**, *115*, 113509.

[30] a) R.-T. Gao, D. He, L. Wu, K. Hu, X. Liu, Y. Su, L. Wang, *Angew. Chem., Int. Ed.* **2020**, *59*, 6213; b) S. Shen, S. A. Lindley, X. Chen, J. Z. Zhang, *Energy Environ. Sci.* **2016**, *9*, 2744; c) R. Siavash Moakhar, S. M. Hosseini-Hosseinabad, S. Masudy-Panah, A. Seza, M. Jalali, H. Fallah-Arani, F. Dabir, S. Gholipour, Y. Abdi, M. Bagheri-Hariri, N. Riahi-Noori, Y.-F. Lim, A. Hagfeldt, M. Saliba, *Adv. Mater.* **2021**, *33*, 2007285; d) Z. Luo, T. Wang, J. Zhang, C. Li, H. Li, J. Gong, *Angew. Chem., Int. Ed.* **2017**, *56*, 12878; e) W. Li, A. Elzatahry, D. Aldhayan, D. Zhao, *Chem. Soc. Rev.* **2018**, *47*, 8203.

[31] a) J. H. Kim, J. S. Lee, *Adv. Mater.* **2019**, *31*, 1806938; b) Z. Wang, C. Li, K. Domen, *Chem. Soc. Rev.* **2019**, *48*, 2109.

[32] a) Y. He, T. Hamann, D. Wang, *Chem. Soc. Rev.* **2019**, *48*, 2182; b) R. Tang, S. Zhou, Z. Zhang, R. Zheng, J. Huang, *Adv. Mater.* **2021**, *33*, 2005389.

[33] J. Zhang, L. Wang, X. Liu, X. A. Li, W. Huang, *J. Mater. Chem. A* **2015**, *3*, 535.

[34] W. Yang, R. R. Prabhakar, J. Tan, S. D. Tilley, J. Moon, *Chem. Soc. Rev.* **2019**, *48*, 4979.

[35] Y. Pihosh, T. Minegishi, V. Nandal, T. Higashi, M. Katayama, T. Yamada, Y. Sasaki, K. Seki, Y. Suzuki, M. Nakabayashi, M. Sugiyama, K. Domen, *Energy Environ. Sci.* **2020**, *13*, 1519.

[36] V. Nandal, Y. Pihosh, T. Higashi, T. Minegishi, T. Yamada, K. Seki, M. Sugiyama, K. Domen, *Energy Environ. Sci.* **2021**, *14*, 4038.

[37] J. Park, W. Yang, J. Tan, H. Lee, J. W. Yun, S. G. Shim, Y. S. Park, J. Moon, *ACS Energy Lett.* **2020**, *5*, 136.

[38] K. Wang, Y. Li, L. Li, C. Wang, Y. Fang, W. Zhao, H. Cai, F. Sun, F. Jiang, *Appl. Catal., B* **2021**, *297*, 120437.

[39] a) S. Chandrasekaran, C. Bowen, P. Zhang, Z. Li, Q. Yuan, X. Ren, L. Deng, *J. Mater. Chem. A* **2018**, *6*, 11078; b) S. Hussain, S. Hussain, A. Waleed, M. M. Tavakoli, Z. Wang, S. Yang, Z. Fan, M. A. Nadeem, *ACS Appl. Mater. Interfaces* **2016**, *8*, 35315; c) S. Hussain, S. Hussain, A. Waleed, M. M. Tavakoli, S. Yang, M. K. Rauf, Z. Fan, M. A. Nadeem, *J. Phys. Chem. C* **2017**, *121*, 18360; d) Y. Liu, F. Le Formal, F. Boudoire, L. Yao, K. Sivula, N. Guijarro, *J. Mater. Chem. A* **2019**, *7*, 1669.

2200181 (30 of 33)

[40] a) J. Ge, Y. Yan, *J. Mater. Chem. C* **2017**, *5*, 6406; b) Y.-X. Yu, L. Pan, M.-K. Son, M. T. Mayer, W.-D. Zhang, A. Hagfeldt, J. Luo, M. Grätzel, *ACS Energy Lett.* **2018**, *3*, 760.

[41] Y. Kuang, Q. Jia, G. Ma, T. Hisatomi, T. Minegishi, H. Nishiyama, M. Nakabayashi, N. Shibata, T. Yamada, A. Kudo, K. Domen, *Nat. Energy* **2016**, *2*, 16191.

[42] a) S. Hu, N. S. Lewis, J. W. Ager, J. Yang, J. R. McKone, N. C. Strandwitz, *J. Phys. Chem. C* **2015**, *119*, 24201; b) D. Bae, B. Seger, P. C. K. Vesborg, O. Hansen, I. Chorkendorff, *Chem. Soc. Rev.* **2017**, *46*, 1933.

[43] S. Huo, Y. Wu, C. Zhao, F. Yu, J. Fang, Y. Yang, *Ind. Eng. Chem. Res.* **2020**, *59*, 14224.

[44] a) Y. Li, R. Wang, H. Li, X. Wei, J. Feng, K. Liu, Y. Dang, A. Zhou, *J. Phys. Chem. C* **2015**, *119*, 20283; b) J. Xiao, X. Zhang, Y. Li, *Int. J. Hydrogen Energy* **2015**, *40*, 9080; c) J. Zhang, Y. Wang, J. Jin, J. Zhang, Z. Lin, F. Huang, J. Yu, *ACS Appl. Mater. Interfaces* **2013**, *5*, 10317.

[45] M. Sun, Z. Chen, X. Jiang, C. Feng, R. Zeng, *J. Alloys Compd.* **2019**, *780*, 540.

[46] M. Crespo-Quesada, L. M. Pazos-Outón, J. Warnan, M. F. Kuehnel, R. H. Friend, E. Reisner, *Nat. Commun.* **2016**, *7*, 12555.

[47] a) J. Kupec, R. L. Stoop, B. Witzigmann, *Opt. Express* **2010**, *18*, 27589; b) R. Asahi, T. Morikawa, T. Ohwaki, K. Aoki, Y. Taga, *Science* **2001**, *293*, 269.

[48] C. Yang, Z. Wang, T. Lin, H. Yin, X. Lü, D. Wan, T. Xu, C. Zheng, J. Lin, F. Huang, X. Xie, M. Jiang, *J. Am. Chem. Soc.* **2013**, *135*, 17831.

[49] B. AlOtaibi, H. P. T. Nguyen, S. Zhao, M. G. Kibria, S. Fan, Z. Mi, *Nano Lett.* **2013**, *13*, 4356.

[50] E. Kim, S. Kim, Y. M. Choi, J. H. Park, H. Shin, *ACS Sustainable Chem. Eng.* **2020**, *8*, 11358.

[51] A. Al-Haddad, Z. Wang, M. Zhou, S. Tarish, R. Vellacheri, Y. Lei, *Small* **2016**, *12*, 5538.

[52] T.-F. Hou, M. A. Johar, R. Boppella, M. A. Hassan, S. J. Patil, S.-W. Ryu, D.-W. Lee, *J. Energy Chem.* **2020**, *49*, 262.

[53] X. Li, A. Liu, D. Chu, C. Zhang, Y. Du, J. Huang, P. Yang, *Catalysts* **2018**, *8*, 108.

[54] a) U. Würfel, A. Cuevas, P. Würfel, *IEEE J. Photovolt.* **2015**, *5*, 461; b) R. Li, F. Zhang, D. Wang, J. Yang, M. Li, J. Zhu, X. Zhou, H. Han, C. Li, *Nat. Commun.* **2013**, *4*, 1432.

[55] D. H. Hong, D. A. Reddy, K. A. J. Reddy, M. Gopannagari, D. P. Kumar, T. K. Kim, *J. Catal.* **2020**, *391*, 471.

[56] A. J. E. Rettie, H. C. Lee, L. G. Marshall, J.-F. Lin, C. Capan, J. Lindemuth, J. S. McCloy, J. Zhou, A. J. Bard, C. B. Mullins, *J. Am. Chem. Soc.* **2013**, *135*, 11389.

[57] G.-Q. Liu, Y. Yang, Y. Li, T. Zhuang, X.-F. Li, J. Wicks, J. Tian, M.-R. Gao, J.-L. Peng, H.-X. Ju, L. Wu, Y.-X. Pan, L.-A. Shi, H. Zhu, J. Zhu, S.-H. Yu, E. H. Sargent, *Nat. Commun.* **2021**, *12*, 4296.

[58] Z. Tian, P. Zhang, P. Qin, D. Sun, S. Zhang, X. Guo, W. Zhao, D. Zhao, F. Huang, *Adv. Energy Mater.* **2019**, *9*, 1901287.

[59] a) I. Grigioni, M. Abdellah, A. Corti, M. V. Dozzi, L. Hammarström, E. Selli, *J. Am. Chem. Soc.* **2018**, *140*, 14042; b) M. S. Sayed, D. Mohapatra, M. L. Baynosa, J. J. Shim, *J. Colloid Interface Sci.* **2021**, *598*, 348.

[60] B. R. Lee, M. G. Lee, H. Park, T. H. Lee, S. A. Lee, S. S. M. Bhat, C. Kim, S. Lee, H. W. Jang, *ACS Appl. Mater. Interfaces* **2019**, *11*, 20004.

[61] Y. Pihosh, V. Nandal, T. Minegishi, M. Katayama, T. Yamada, K. Seki, M. Sugiyama, K. Domen, *ACS Energy Lett.* **2020**, *5*, 2492.

[62] a) H. Zhang, L. Ma, J. Ming, B. Liu, Y. Zhao, Y. Hou, Z. Ding, C. Xu, Z. Zhang, J. Long, *Appl. Catal., B: Environ.* **2019**, *243*, 481; b) H.-I. Kim, D. Monllor-Satoca, W. Kim, W. Choi, *Energy Environ. Sci.* **2015**, *8*, 247.

[63] M. Fang, G. Dong, R. Wei, J. C. Ho, *Adv. Energy Mater.* **2017**, *7*, 1700559.

[64] a) F. Wu, Y. Yu, H. Yang, L. N. German, Z. Li, J. Chen, W. Yang, L. Huang, W. Shi, L. Wang, X. Wang, *Adv. Mater.* **2017**, *29*, 1701432; b) T. Fang, H. Hu, J. Liu, M. Jiang, S. Zhou, J. Fu, W. Wang, Y. Yang, *J. Phys. Chem. C* **2021**, *125*, 18734; c) X. Guan, J. Becdelievre, B. Meunier, A. Benali, G. Saint-Girons, R. Bachelet, P. Regreny, C. Botella, G. Grenet, N. P. Blanchard, X. Jaurand, M. G. Silly, F. Sirotti, N. Chauvin, M. Gendry, J. Penuelas, *Nano Lett.* **2016**, *16*, 2393; d) Y. He, P. Shen, Y. Liu, M. Chen, D. Cao, X. Yan, *Mater. Sci. Semicond. Process.* **2021**, *121*, 105351; e) W. Zhao, Q. Zhang, H. Wang, J. Rong, L, E, Y. Dai, *Nano Energy* **2020**, *73*, 104783.

[65] a) Z. Wang, D. Cao, L. Wen, R. Xu, M. Obergfell, Y. Mi, Z. Zhan, N. Nasori, J. Demsar, Y. Lei, *Nat. Commun.* **2016**, *7*, 10348; b) D. Cao, Z. Wang, Nasori, L. Wen, Y. Mi, Y. Lei, *Angew. Chem., Int. Ed.* **2014**, *53*, 11027

[66] W. Yang, Y. Yu, M. B. Starr, X. Yin, Z. Li, A. Kvit, S. Wang, P. Zhao, X. Wang, *Nano Lett.* **2015**, *15*, 7574.

[67] a) J. Huang, Y. Wang, X. Liu, Y. Li, X. Hu, B. He, Z. Shu, Z. Li, Y. Zhao, *Nano Energy* **2019**, *59*, 33; b) Y. He, J. Zhu, Y. Yuan, M. Li, Y. Yang, Y. Liu, M. Chen, D. Cao, X. Yan, *J. Mater. Chem. A* **2021**, *9*, 7594.

[68] a) J. Yang, D. Wang, H. Han, C. Li, *Acc. Chem. Res.* **2013**, *46*, 1900; b) Y. Zhao, X. Jia, G. Chen, L. Shang, G. I. N. Waterhouse, L.-Z. Wu, C.-H. Tung, D. O'Hare, T. Zhang, *J. Am. Chem. Soc.* **2016**, *138*, 6517.

[69] F. A. L. Laskowski, M. R. Nellist, J. Qiu, S. W. Boettcher, *J. Am. Chem. Soc.* **2019**, *141*, 1394.

[70] a) Y. F. Tay, H. Kaneko, S. Y. Chiam, S. Lie, Q. Zheng, B. Wu, S. S. Hadke, Z. Su, P. S. Bassi, D. Bishop, T. C. Sum, T. Minegishi, J. Barber, K. Domen, L. H. Wong, *Joule* **2018**, *2*, 537; b) J. Yan, S. Wu, X. Zhai, X. Gao, X. Li, *J. Power Sources* **2017**, *342*, 460.

[71] a) J. Gu, J. A. Aguiar, S. Ferrere, K. X. Steirer, Y. Yan, C. Xiao, J. L. Young, M. Al-Jassim, N. R. Neale, J. A. Turner, *Nat. Energy* **2017**, *2*, 16192; b) L. Guo, P. S. Shinde, Y. Ma, L. Li, S. Pan, F. Yan, *Sol. RRL* **2020**, *4*, 1900442.

[72] a) K. Wang, Z. Xing, D. Meng, S. Zhang, Z. Li, K. Pan, W. Zhou, *Appl. Catal., B* **2021**, *281*, 119482; b) S. Deng, F. Yang, Q. Zhang, Y. Zhong, Y. Zeng, S. Lin, X. Wang, X. Lu, C.-Z. Wang, L. Gu, X. Xia, J. Tu, *Adv. Mater.* **2018**, *30*, 1802223.

[73] P. Chakthranont, T. R. Hellstern, J. M. McEnaney, T. F. Jaramillo, *Adv. Energy Mater.* **2017**, *7*, 1701515.

[74] a) H. W. Liang, S. Brüller, R. Dong, J. Zhang, X. Feng, K. Müllen, *Nat. Commun.* **2015**, *6*, 7992; b) A. Shahraei, I. Martinaiou, K. A. Creutz, M. Kübler, N. Weidler, S. T. Ranecky, W. D. Z. Wallace, M. A. Nowroozi, O. Clemens, R. W. Stark, U. I. Kramm, *Chem. Eur. J.* **2018**, *24*, 12480; c) A. Shahraei, A. Moradabadi, I. Martinaiou, S. Lauterbach, S. Klemenz, S. Dolique, H. J. Kleebe, P. Kaghazchi, U. I. Kramm, *ACS Appl. Mater. Interfaces* **2017**, *9*, 25184.

[75] a) W. Li, D. He, S. W. Sheehan, Y. He, J. E. Thorne, X. Yao, G. W. Brudvig, D. Wang, *Energy Environ. Sci.* **2016**, *9*, 1794; b) J. Seo, T. Takata, M. Nakabayashi, T. Hisatomi, N. Shibata, T. Minegishi, K. Domen, *J. Am. Chem. Soc.* **2015**, *137*, 12780; c) L. Reith, C. A. Triana, F. Pazoki, M. Amiri, M. Nyman, G. R. Patzke, *J. Am. Chem. Soc.* **2021**, *143*, 15022.

[76] C. Li, Z. Chen, W. Yuan, Q.-H. Xu, C. M. Li, *Nanoscale* **2019**, *11*, 1111.

[77] B. He, Y. Wang, X. Liu, Y. Li, X. Hu, J. Huang, Y. Yu, Z. Shu, Z. Li, Y. Zhao, *J. Mater. Chem. A* **2019**, *7*, 6747.

[78] a) R. Chen, C. Zhen, Y. Yang, X. Sun, J. T. S. Irvine, L. Wang, G. Liu, H.-M. Cheng, *Nano Energy* **2019**, *59*, 683; b) K. R. Nandanapalli, D. Mudusu, J.-S. Yu, S. Lee, *J. Colloid Interface Sci.* **2020**, *558*, 9; c) J. Yang, K. Walczak, E. Anzenberg, F. M. Toma, G. Yuan, J. Beeman, A. Schwartzberg, Y. Lin, M. Hettick, A. Javey,

J. W. Ager, J. Yano, H. Frei, I. D. Sharp, *J. Am. Chem. Soc.* **2014**, *136*, 6191.

[79] a) L. Wu, L. Wang, J. Zhu, M. Sun, X. Liu, P. Schmuki, J. Zhang, *J. Mater. Chem. A* **2020**, *8*, 2563; b) S. Hu, C. Xiang, S. Haussener, A. D. Berger, N. Lewis, *Energy Environ. Sci.* **2013**, *6*, 2984.

[80] a) H. Zhang, S. Huang, G. Conibeer, *Energy Procedia* **2012**, *22*, 10; b) M. M. May, H.-J. Lewerenz, D. Lackner, F. Dimroth, T. Hannappel, *Nat. Commun.* **2015**, *6*, 8286.

[81] Q. Wang, T. Hisatomi, Q. Jia, H. Tokudome, M. Zhong, C. Wang, Z. Pan, T. Takata, M. Nakabayashi, N. Shibata, Y. Li, I. D. Sharp, A. Kudo, T. Yamada, K. Domen, *Nat. Mater.* **2016**, *15*, 611.

[82] M. Gratzel, *Nature* **2001**, *414*, 338.

[83] a) Q. Chen, G. Fan, H. Fu, Z. Li, Z. Zou, *Adv. Phys.: X* **2018**, *3*, 1487267. b) M. T. Spitler, M. A. Modestino, T. G. Deutsch, C. X. Xiang, J. R. Durrant, D. V. Esposito, S. Haussener, S. Maldonado, I. D. Sharp, B. A. Parkinson, D. S. Ginley, F. A. Houle, T. Hannappel, N. R. Neale, D. G. Nocera, P. C. McIntyre, *Sustainable Energy Fuels* **2020**, *4*, 985.

[84] L. C. Kao, S. Y. H. Liou, C. L. Dong, P. H. Yeh, C. L. Chen, *ACS Sustainable Chem. Eng.* **2016**, *4*, 210.

[85] G. Wang, X. Yang, F. Qian, J. Z. Zhang, Y. Li, *Nano Lett.* **2010**, *10*, 1088.

[86] W.-H. Cheng, M. H. Richter, M. M. May, J. Ohlmann, D. Lackner, F. Dimroth, T. Hannappel, H. A. Atwater, H.-J. Lewerenz, *ACS Energy Lett.* **2018**, *3*, 1795.

[87] I. Y. Ahmet, S. Berglund, A. Chemseddine, P. Bogdanoff, R. F. Präg, F. F. Abdi, R. van de Krol, *Adv. Energy Sustainability Res.* **2020**, *1*, 2000037.

[88] K. Xu, A. Chatzitakis, E. Vøllestad, Q. Ruan, J. Tang, T. Norby, *Int. J. Hydrogen Energy* **2019**, *44*, 587.

[89] K. Xu, A. Chatzitakis, T. Norby, *Photochem. Photobiol. Sci.* **2017**, *16*, 10.

[90] F. Li, K. Fan, B. Xu, E. Gabrielsson, Q. Daniel, L. Li, L. Sun, *J. Am. Chem. Soc.* **2015**, *137*, 9153.

[91] Y. Wang, H. Shi, K. Cui, L. Zhang, S. Ge, J. Yu, *Appl. Catal., B* **2020**, *275*, 129.

[92] Y.-H. Lai, D. W. Palm, E. Reisner, *Adv. Energy Mater.* **2015**, *5*, 1501668.

[93] B. Shan, M. K. Brennaman, L. Troian-Gautier, Y. Liu, A. Nayak, C. M. Klug, T. T. Li, R. M. Bullock, T. J. Meyer, *J. Am. Chem. Soc.* **2019**, *141*, 10390.

[94] Y. H. Lai, K. C. Lin, C. Y. Yen, B. J. Jiang, *Faraday Discuss.* **2019**, *215*, 297.

[95] A. Paracchino, V. Laporte, K. Sivula, M. Grätzel, E. Thimsen, *Nat. Mater.* **2011**, *10*, 456.

[96] P. Bornoz, F. F. Abdi, S. D. Tilley, B. Dam, R. van de Krol, M. Graetzel, K. Sivula, *J. Phys. Chem. C* **2014**, *118*, 16959.

[97] X. Fu, H. Chang, Z. Shang, P. Liu, J. Liu, H. Luo, *Chem. Eng. J.* **2020**, *381*, 122001.

[98] M. H. Tran, T. Schäfer, A. Shahraei, M. Dürrschnabel, L. Molina-Luna, U. I. Kramm, C. S. Birkel, *ACS Appl. Energy Mater.* **2018**, *1*, 3908.

[99] M. Naguib, O. Mashtalir, J. Carle, V. Presser, J. Lu, L. Hultman, Y. Gogotsi, M. W. Barsoum, *ACS Nano* **2012**, *6*, 1322.

[100] L. Pan, J. H. Kim, M. T. Mayer, M.-K. Son, A. Ummadisingu, J. S. Lee, A. Hagfeldt, J. Luo, M. Grätzel, *Nat. Catal.* **2018**, *1*, 412.

[101] N. Kaneza, P. S. Shinde, Y. Ma, S. Pan, *RSC Adv.* **2019**, *9*, 13576.

[102] J. Liu, Y. Zhang, Z. Bai, Z. Huang, Y. Gao, Y. Yao, *Nano* **2019**, *14*, 1950146.

[103] X. Yin, Q. Liu, Y. Yang, Y. Liu, K. Wang, Y. Li, D. Li, X. Qiu, W. Li, J. Li, *Int. J. Hydrogen Energy* **2019**, *44*, 594.

[104] J. J. Leung, J. Warnan, D. H. Nam, J. Z. Zhang, J. Willkomm, E. Reisner, *Chem. Sci.* **2017**, *8*, 5172.

[105] J. W. Jang, C. Du, Y. Ye, Y. Lin, X. Yao, J. Thorne, E. Liu, G. McMahon, J. Zhu, A. Javey, J. Guo, D. Wang, *Nat. Commun.* **2015**, *6*, 7447.

[106] D. Xue, M. Kan, X. Qian, Y. Zhao, *ACS Sustainable Chem. Eng.* **2018**, *6*, 16228.

[107] B. Seger, T. Pedersen, A. B. Laursen, P. C. K. Vesborg, O. Hansen, I. Chorkendorff, *J. Am. Chem. Soc.* **2013**, *135*, 1057.

[108] Y. Yang, S. Ciampi, M. H. Choudhury, J. J. Gooding, *J. Phys. Chem. C* **2016**, *120*, 2874.

[109] Y. Wu, Z. Yue, A. Liu, P. Yang, M. Zhu, *ACS Sustainable Chem. Eng.* **2016**, *4*, 2569.

[110] A. Sharma, P. Sahoo, A. Singha, S. Padhan, R. Thangavel, *Mater. Sci. Semicond. Process.* **2021**, *121*, 105433.

[111] V. Andrei, R. L. Z. Hoye, M. Crespo-Quesada, M. Bajada, S. Ahmad, M. De Volder, R. Friend, E. Reisner, *Adv. Energy Mater.* **2018**, *8*, 1801403.

[112] E. E. Moore, V. Andrei, S. Zacarias, I. A. C. Pereira, E. Reisner, *ACS Energy Lett.* **2020**, *5*, 232.

[113] R. Sathre, C. D. Scown, W. R. Morrow, J. C. Stevens, I. D. Sharp, J. W. Ager, K. Walczak, F. A. Houle, J. B. Greenblatt, *Energy Environ. Sci.* **2014**, *7*, 3264.

[114] S. Linic, U. Aslam, C. Boerigter, M. Morabito, *Nat. Mater.* **2015**, *14*, 567.

[115] M. Rycenga, C. M. Cobley, J. Zeng, W. Li, C. H. Moran, Q. Zhang, D. Qin, Y. Xia, *Chem. Rev.* **2011**, *111*, 3669.

[116] Y.-G. Lin, Y.-K. Hsu, Y.-C. Chen, S.-B. Wang, J. T. Miller, L.-C. Chen, K.-H. Chen, *Energy Environ. Sci.* **2012**, *5*, 8917.

[117] A. Sobhani, M. W. Knight, Y. Wang, B. Zheng, N. S. King, L. V. Brown, Z. Fang, P. Nordlander, N. J. Halas, *Nat. Commun.* **2013**, *4*, 1643.

[118] W. R. Erwin, H. F. Zarick, E. M. Talbert, R. Bardhan, *Energy Environ. Sci.* **2016**, *9*, 1577.

[119] Y. Liu, F. Ren, S. Shen, Y. Fu, C. Chen, C. Liu, Z. Xing, D. Liu, X. Xiao, W. Wu, X. Zheng, Y. Liu, C. Jiang, *Appl. Phys. Lett.* **2015**, *106*, 123901.

[120] J. Li, S. K. Cushing, P. Zheng, T. Senty, F. Meng, A. D. Bristow, A. Manivannan, N. Wu, *J. Am. Chem. Soc.* **2014**, *136*, 8438.

[121] R. Xu, L. Wen, Z. Wang, H. Zhao, S. Xu, Y. Mi, Y. Xu, M. Sommerfeld, Y. Fang, Y. Lei, *ACS Nano* **2017**, *11*, 7382.

[122] Y. C. Lin, L. C. Hsu, C. Y. Lin, C. L. Chiang, C. M. Chou, W. W. Wu, S. Y. Chen, Y. G. Lin, *ACS Appl. Mater. Interfaces* **2019**, *11*, 38625.

[123] H. Hu, L. Wu, Y. Tan, Q. Zhong, M. Chen, Y. Qiu, D. Yang, B. Sun, Q. Zhang, Y. Yin, *J. Am. Chem. Soc.* **2018**, *140*, 406.

[124] M. Chen, Y. Zou, L. Wu, Q. Pan, D. Yang, H. Hu, Y. Tan, Q. Zhong, Y. Xu, H. Liu, B. Sun, Q. Zhang, *ACS Appl. Mater. Interfaces* **2017**, *27*, 1701121.

[125] F. Liu, S. Goyal, M. Forrester, T. Ma, K. Miller, Y. Mansoorieh, J. Henjum, L. Zhou, E. Cochran, S. Jiang, *Nano Lett.* **2019**, *19*, 1587.

[126] R. Fu, L. Li, X. Li, B. Li, C. Shao, Z. Liu, A. Shen, *Mater. Chem. Phys.* **2021**, *267*, 129.

Zhijie Wang received his BS degree in 2004 from Zhejiang University and PhD degree in 2009 from the Institute of Semiconductors, Chinese Academy of Sciences. He has postdoc experiences in in the University of Wyoming, the University of Michigan, and the Technical University of Ilmenau. He is currently a professor in the Institute of Semiconductors, Chinese Academy of Sciences. His research interest includes nanomaterials, nano-devices, energy-related sciences, surface science, and photoelectrochemistry.

Yong Lei is Professor and Head of Group (Chair) of Applied Nano-Physics at the Technical University of Ilmenau, Germany. He started to work in Germany as an Alexander von Humboldt Fellow at Karlsruhe Institute of Technology in 2003. From 2006 he worked at University of Muenster as a group leader and Junior Professor. In 2011 he joined the Technical University of Ilmenau as a Chair Professor. His research focuses include template nanostructuring, energy conversion and storage devices, and optoelectronic applications of functional nanostructures. He received a few prestigious funding in Europe and Germany such as two European Research Council Grants. Prof. Lei is Advisory Board Member or Associate Editor of a few journals such as *Advanced Energy Materials*, *Energy & Environmental Materials*, *InfoMat* and *Carbon Energy*.